Available online at www.sciencedirect.com
ScienceDirect
Comput. Methods Appl. Mech. Engrg. 417 (2023) 116439
Computer methods in applied mechanics and engineering
www.elsevier.com/locate/cma

11-th order of accuracy for numerical solution of 3-D Poisson equation with irregular interfaces on unfitted Cartesian meshes

A. Idesman[a,*], M. Mobin[a], J. Bishop[b]

[a] *Department of Mechanical Engineering, Texas Tech University, Lubbock, TX 79409-1021, USA*
[b] *Engineering Sciences Center, Sandia National Laboratories, Albuquerque, NM 87185, USA*

Received 9 May 2023; received in revised form 19 August 2023; accepted 5 September 2023
Available online xxxx

Abstract

For the first time the optimal local truncation error method (OLTEM) with 125-point stencils and unfitted Cartesian meshes has been developed in the general 3-D case for the Poisson equation for heterogeneous materials with smooth irregular interfaces. The 125-point stencils equations that are similar to those for quadratic finite elements are used for OLTEM. The interface conditions for OLTEM are imposed as constraints at a small number of interface points and do not require the introduction of additional unknowns, i.e., the sparse structure of global discrete equations of OLTEM is the same for homogeneous and heterogeneous materials. The stencils coefficients of OLTEM are calculated by the minimization of the local truncation error of the stencil equations. These derivations include the use of the Poisson equation for the relationship between the different spatial derivatives. Such a procedure provides the maximum possible accuracy of the discrete equations of OLTEM. In contrast to known numerical techniques with quadratic elements and third order of accuracy on conforming and unfitted meshes, OLTEM with the 125-point stencils provides 11-th order of accuracy, i.e., an extremely large increase in accuracy by 8 orders for similar stencils. The numerical results show that OLTEM yields much more accurate results than high-order finite elements with much wider stencils. The increased numerical accuracy of OLTEM leads to an extremely large increase in computational efficiency.

Also, a new post-processing procedure with the 125-point stencil has been developed for the calculation of the spatial derivatives of the primary function. The post-processing procedure includes the minimization of the local truncation error and the use of the Poisson equation. It is demonstrated that the use of the partial differential equation (PDE) for the 125-point stencils improves the accuracy of the spatial derivatives by 6 orders compared to post-processing without the use of PDE as in existing numerical techniques. At an accuracy of 0.1% for the spatial derivatives, OLTEM reduces the number of degrees of freedom by $900 - 4 \cdot 10^6$ times compared to quadratic finite elements. The developed post-processing procedure can be easily extended to unstructured meshes and can be independently used with existing post-processing techniques (e.g., with finite elements).

Keywords: Poisson equation; Heterogeneous materials; Smooth irregular interfaces; Unfitted Cartesian meshes; Optimal accuracy; Post-processing; Spatial derivatives

* Corresponding author.
E-mail addresses: alexander.idesman@ttu.edu (A. Idesman), mmobin@ttu.edu (M. Mobin), jebisho@sandia.gov (J. Bishop).

https://doi.org/10.1016/j.cma.2023.116439
0045-7825/

1. Introduction

The Poisson equation for heterogeneous materials with interfaces is used for the description of many important phenomena such as heat transfer, multiphase flows, neurosciences, electrostatics and many others. Therefore, many efforts are made for the development of accurate and computationally efficient numerical techniques for this equation, e.g., see [1–16] and others. Many of these recent publications consider numerical techniques with unfitted meshes. The use of unfitted meshes for irregular interfaces significantly simplifies the preparation of input data for numerical simulations because the generation of conforming meshes for complex irregular interfaces may lead to poor quality elements (e.g., the elements with small angles) and reduced accuracy of numerical results. One of the popular numerical approaches for heterogeneous materials with unfitted meshes is based on different modifications of the finite element method, e.g., the cut finite element method, the finite cell method, generalized finite element method, extended finite element method, immersed finite element method, shifted interface method and others (see [3,5,7–12,14–16]). These methods provide the same $p+1$ order of accuracy as that for finite elements with conforming meshes where p is the order of finite elements. Another interesting numerical approach for heterogeneous materials with unfitted Cartesian meshes is related to modifications of the immersed interface method that is based on the finite difference approximations of the partial derivatives, e.g., see [17–22] and others. Some of these techniques provide fourth and sixth orders of accuracy for the Poisson equation with interfaces (e.g., see [19,22]). However, they require special approximations of the normal derivatives for the stencils located close to curved interfaces. This leads to an increase in the stencil width for the grid points located close to the interface. Due to a large number of possible locations of the interface with respect to grid points, the implementation of such techniques is difficult for a high order of accuracy especially in the 3-D case.

Recently we have developed OLTEM with compact stencils for the solution of different PDEs on regular and irregular domains and interfaces with unfitted Cartesian meshes (e.g., see [23–32]). OLTEM provides the maximum possible accuracy of discrete equations after the space discretization of the corresponding PDEs. In contrast to finite elements, OLTEM with similar stencils provides different orders of accuracy for different PDEs (e.g., see [23–32]). In our paper [30] we showed that OLTEM with $5\times 5=25$-point stencils (similar to those for quadratic finite elements) for the 2-D Poisson equation on regular domains with conforming Cartesian meshes and homogeneous materials provides the 18th order of accuracy, i.e., increase by 15 orders compared to quadratic finite elements. In our paper [31] we have developed OLTEM with $3\times 3=9$-point and $5\times 5=25$-point stencils (similar to those for linear and quadratic finite elements) and unfitted Cartesian meshes for the 2-D Poisson equation for heterogeneous materials with smooth irregular interfaces. We showed that the maximum possible accuracy of OLTEM with the 9-point and 25-point stencils in this case is 3 and 11, respectively, i.e., compared to linear and quadratic finite elements, OLTEM improves accuracy by one and 8 orders, respectively. In our paper [32] we have developed OLTEM with $3\times 3\times 3=27$-point stencils (similar to those for linear finite elements) for the 3-D Poisson equation for heterogeneous materials with irregular interfaces, and we have obtained the 3-rd order of accuracy (similar to OLTEM in the 2-D case; see [31]). In our paper [32] we have also developed a new post-processing procedure that improves the accuracy for the calculation of the spatial derivatives of primary functions by the use of the original PDEs.

The main objectives of this paper are to develop OLTEM with $5\times 5\times 5=125$-point stencils (similar to those for quadratic finite elements) for the 3-D Poisson equation for heterogeneous materials with smooth irregular interfaces and to show that in the general 3-D case OLTEM can provide an extremely large increase in accuracy compared to that for quadratic finite elements. The second objective is to develop the post-processing procedure for the calculation of the spatial derivatives of primary functions that significantly improves the accuracy of the spatial derivatives compared to that for known approaches. The post processing procedure is also based on the $5\times 5\times 5=125$-point stencils and on the use of the original PDE. The derivations in Section 4 show that the use of the Poisson equation for post-processing with the 125-point stencils improves the accuracy of the spatial derivatives by 6 orders. We should mention that the development of OLTEM with the 125-point stencils in the 3-D case is a challenging problem due to a large number of the stencil coefficients (125 stencil coefficients) used for each stencil and for the derivation of the corresponding formulas. For example, we have found that by zeroing some of the 125 stencil coefficients we can significantly simplify the formulas without the reduction in the order of accuracy of OLTEM; see Sections 3.1.1, 3.1.2 and 4 below. It is also interesting to mention that at the development of OLTEM with the 125-point stencils for heterogeneous materials, we have found interesting results for homogeneous materials (a particular case of general heterogeneous materials). It occurs that the maximum possible order of accuracy of

OLTEM with the 125-point stencils for homogeneous materials in the 3-D case is 14, i.e., it is 4 orders lower compared to that for OLTEM with $5 \times 5 = 25$-point stencils (corresponding to quadratic finite elements) in the 2-D case; see our paper [30]. However, because the accuracy of OLTEM for heterogeneous materials is defined by the lowest accuracy of the heterogeneous stencils (when the 125-point cells are intersected by interfaces), the 11th order of accuracy of OLTEM with 125-point stencils is the same in the 2-D and 3-D cases. This order of accuracy of OLTEM significantly (by 8 orders) exceeds that of the existing numerical techniques with similar stencils (corresponding to quadratic elements) for heterogeneous materials on conforming and unfitted meshes, e.g. see [3,5,7–12,14–16].

The paper is organized as follows. The 3-D Poisson equation for heterogeneous materials with irregular interfaces as well as the introduction of the local truncation error for stencils equations are presented in Section 2. In Section 3.1, OLTEM with the 125-point stencils is derived for the 3-D Poisson equation with discontinuous coefficients and zero source term. Its extension to nonzero source term is considered in Section 3.2. The development of OLTEM for the calculation of the spatial derivatives of numerical solutions (post-processing) is presented in Section 4. Numerical examples for 3-D domains with irregular interfaces and unfitted Cartesian meshes as well as the comparison with FEM are presented in Section 5. For the derivation of many analytical expressions presented below, we use the computational program Mathematica [33].

2. 3-D Poisson equation for heterogeneous materials and the local truncation error

The Poisson equation in a composite domain $\Omega = \cup\Omega_l$ ($l = 1, 2, \ldots, \bar{N}$ where $\bar{N}$ is the total number of subdomains) can be written down in each subdomain Ω_l as follows:

$$c_l \nabla^2 u_l = f_l\,, \qquad l = 1, 2, \ldots, \bar{N} \tag{1}$$

where c_l is the material constant for each subdomain Ω_l and can be discontinuous across the interfaces between subdomains, $f_l(\boldsymbol{x})$ is the source term that can be also discontinuous across the interfaces between subdomains Ω_l, u_l is the field variable. We also assume that the functions u_l and f_l are sufficiently smooth in each subdomain Ω_l. In this paper the Dirichlet boundary conditions $u = g_1$ are applied along the boundary Γ where g_1 is the given function. However, the Neumann boundary conditions can be also used with the proposed approach, e.g., see our paper [28]. At the interface G between any two subdomains, the following interface conditions are applied:

$$u_G^* - u_G^{**} = \delta_1\,, \qquad c_*(n_x \frac{\partial u_G^*}{\partial x} + n_y \frac{\partial u_G^*}{\partial y} + n_z \frac{\partial u_G^*}{\partial z}) - c_{**}(n_x \frac{\partial u_G^{**}}{\partial x} + n_y \frac{\partial u_G^{**}}{\partial y} + n_z \frac{\partial u_G^{**}}{\partial z}) = \delta_2\,, \tag{2}$$

where $\delta_1(x, y, z)\ |_{(x,y,z)\in G}$ and $\delta_2(x, y, z)\ |_{(x,y,z)\in G}$ are the given jumps for the function and the flux across the interface, n_x, n_y and n_z are the x-, y- and z-components of the normal vector at the interface, c_* (c_{**}) is the corresponding material constant, and the symbols $*$ and $**$ correspond to the quantities on the opposite sides from the interface for the corresponding subdomains Ω_l. For zero jumps $\delta_1(x, y, z) = \delta_2(x, y, z) = 0$, the functions u_l are continuous across the interfaces but can have the discontinuous spatial derivatives across the interfaces.

In OLTEM, the discrete system for the Poisson equation after the spatial discretization with a Cartesian rectangular mesh can be represented as a system of algebraic equations. The algebraic equation of this system for each internal grid point of the domain is called the stencil equation and can be written down for the case without interfaces as follows:

$$\sum_{i=1}^{M} k_i u_i^{\text{num}} = \bar{f}\,, \tag{3}$$

where u_i^{num} is the numerical solution for function u at the ith grid point, k_i are the unknown stencil coefficients to be determined, $\bar{f}$ is the discretized source term (see the next Sections and Eq. (25)), M is the number of the grid points included into the stencil equation. Many numerical techniques such as the finite difference method, the finite element method, the finite volume method, the isogeometric elements, the spectral elements, meshless methods, and others can ultimately be reduced to Eq. (3) with some specific coefficients k_i. In the derivations below, we will assume $5 \times 5 \times 5 = 125$-point ($M = 125$) stencils in the 3-D case that are similar to the 125-point stencils of 3-D quadratic quadrilateral finite elements on Cartesian meshes. Generally, stencils with any number of points M can be used.

Let us introduce the local truncation error used with OLTEM. The replacement of the numerical values of function u_i^{num} at the grid points in Eq. (3) by the exact solution u_i to the Poisson equation, Eq. (1), leads to the residual e of this equation called the local truncation error of the discrete equation, Eq. (3):

$$e = \sum_{i=1}^{M} k_i u_i - \bar{f} \,. \tag{4}$$

Calculating the difference between Eqs. (4) and (3) we can get

$$e = \sum_{i=1}^{M} k_i [u_i - u_i^{\text{num}}] = \sum_{i=1}^{M} k_i \bar{e}_i^u \,, \tag{5}$$

where $\bar{e}_i^u = u_i - u_i^{\text{num}}$ are the errors of function u_i at the grid points i. As can be seen from Eq. (5), the local truncation error e is a linear combination of the errors of the function u at the grid points i that are included into the stencil equation.

3. OLTEM for the 3-D Poisson equation with discontinuous coefficients

OLTEM with the 125-point stencils for the 3-D Poisson equations with interfaces will be first derived for zero source term $f_l = 0$. The derivation includes the introduction of the local truncation error for heterogeneous stencils, the modification of the local truncation error by the addition of the interface conditions at a small number of interface points as constraints, and the calculation of the stencil coefficients by the minimization of the local truncation error. Then, the extension of OLTEM to non-zero source term $f_l \neq 0$ will be presented. The non-zero source term does not affect the calculation of the stencil coefficients and only contributes to the calculation of the right-hand side of the stencil equation.

3.1. Zero source term $f_l = 0$

Consider a 3-D bounded domain and a Cartesian mesh with a mesh size h where h is the size of the mesh along the x-axis, $b_y h$, $b_z h$ are the sizes of the mesh along the $y-$ and $z-$axes (b_y and b_z are the aspect ratios of the mesh). To simplify derivations, below we consider domains with rectangular boundary and irregular interfaces between different materials. However, irregular domains can be also considered with OLTEM (see [23,25,34]). In the paper we will consider the 125-point uniform stencils that are similar to those for quadratic quadrilateral finite elements. We use the same structure of stencils for homogeneous and heterogeneous materials (the difference between homogeneous and heterogeneous stencils is in the values of the stencil coefficients only). The spatial locations of the 124 grid points that are close to the internal grid point $i = 63$ and contribute to the 125-point stencil for this grid point are shown in Fig. 1. For convenience, the local numeration of the grid points from 1 to 125 is used in Fig. 1 as well as in the derivations below. If all grid points of the 125-point stencil belong to the same material than this stencil is treated as that for homogeneous materials (see Fig. 1a) otherwise as for heterogeneous materials (see Fig. 1b).

The interface in Fig. 1b divides the 125-point uniform stencil into two parts with different material properties. In order to impose the interface conditions at the interface, we select a small number of interface points as follows. First we select one point at the interface with the coordinates $x_G = x_{G,1}$, $y_G = y_{G,1}$ and $z_G = z_{G,1}$. This point can be selected as the shortest distance from the central grid point $i = 63$ of the 125-point stencil to the interface. Then, we additionally select 80 interface points in two perpendicular directions, i.e., we use totally $N_G = 9 \times 9 = 81$ interface points for each stencil with interfaces. We select the same distances $\bar{h} = \sqrt{(x_{G,j} - x_{G,i})^2 + (y_{G,j} - y_{G,i})^2 + (z_{G,j} - z_{G,i})^2}$ between the interface points where i and j designate the neighboring interface points, see Fig. 1b (we do not show all 81 interface points in Fig. 1b). Numerical experiments show that small distances $\bar{h} = h/5$ yield accurate results. Note that existing mesh generators can be used for finding the coordinates of the 81 interface points. For example, a mesh generator can discretize the interface in the vicinity of the first interface point with the coordinates $x_G = x_{G,1}$, $y_G = y_{G,1}$, $z_G = z_{G,1}$ and can create 80 additional interface points with approximately the same distances between them.

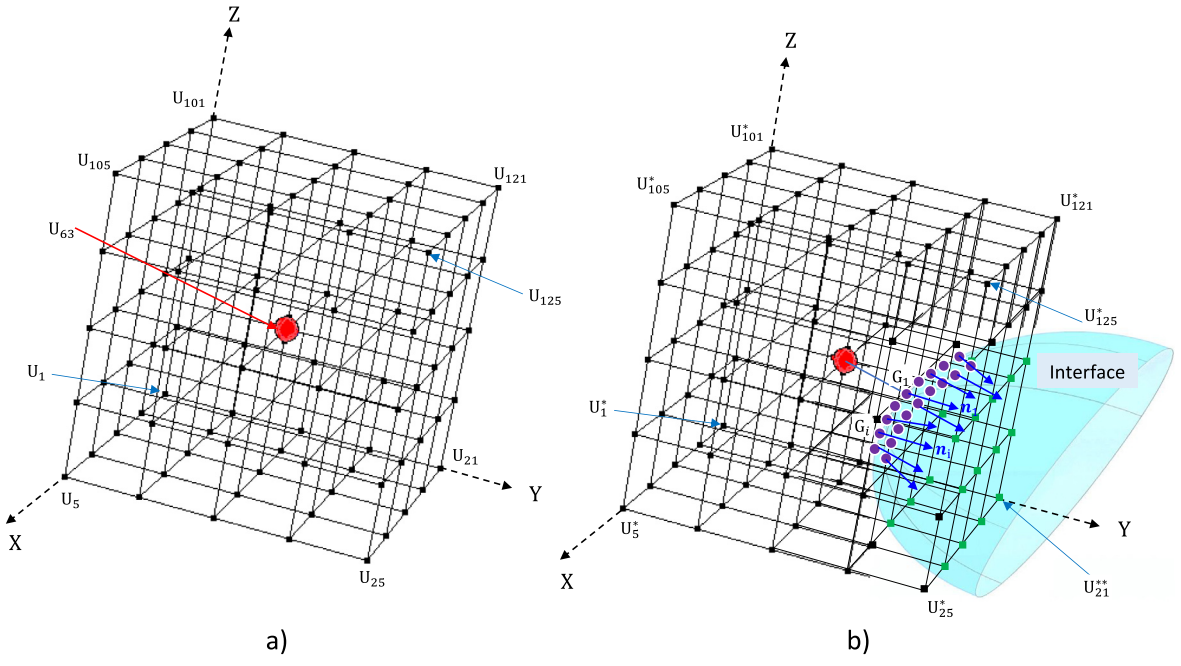

Fig. 1. The spatial locations of the grid points i ($i = 1, 2, \ldots, 125$) that contribute to the 125-point uniform stencil for the internal grid point $i = 63$ for homogeneous material without interface (a) and for heterogeneous material with interface (b). The red point is the central grid point of the 125-point stencil, black and green points correspond to the regular Cartesian grid points with different material properties, purple points G_i correspond to the selected interface points with the normal vectors $\boldsymbol{n}_i$. (For interpretation of the references to color in this figure legend, the reader is referred to the web version of this article.)

Let us describe the coordinates of the grid points of the 125 point uniform stencils (see Fig. 1) with respect to their central point u_{63} as follow:

$$x_p = x_{63} + r_{x,p}h = x_{63} + (i-3)h\,, \qquad y_p = y_{63} + r_{y,p}b_y h = y_{63} + (j-3)b_y h\,,$$
$$z_p = z_{63} + r_{z,p}b_z h = z_{63} + (t-3)b_z h\,, \tag{6}$$

where the coefficients $r_{x,p}$, $r_{y,p}$, $r_{z,p}$ are:

$$r_{x,p} = (i-3)\,, \qquad r_{y,p} = (j-3)\,, \qquad r_{z,p} = (t-3)\,, \tag{7}$$

and $p = 25(t-1) + 5(j-1) + i$ with $i, j, t = 1, 2, 3, 4, 5$.

To describe the coordinates of the selected N_G points on the interface (see Fig. 1b) we introduce $3N_G$ coefficients $d_{x,p}$, $d_{y,p}$ and $d_{z,p}$ ($p = 1, 2, \ldots, N_G$) with $N_G = 81$ for the 125-point stencil as follows (see also Fig. 1b):

$$x_{G,j} = x_G + d_{x,j}h\,, \qquad y_{G,j} = y_G + d_{y,j}b_y h\,, \qquad z_{G,j} = z_G + d_{z,j}b_z h\,, \qquad j = 1, 2, \ldots, N_G\,, \tag{8}$$

where $d_{x,1} = d_{y,1} = d_{z,1} = 0$ for the central interface point $G = G_1$ with the coordinates $x_G = x_{G,1}$, $y_G = y_{G,1}$ and $z_G = z_{G,1}$ (see Fig. 1b).

Remark 1. Some of the interface points G_i ($i = 1, 2, \ldots, N_G$) can be located outside the 125-point cells. The derivations presented below are also valid for these cases. This scenario is implemented in our code used for all numerical results in Section 5.

The stencil equation, Eq. (3), for heterogeneous materials with the 125-point uniform stencil for the grid point u_{63} (see Fig. 1) is assumed to be in the following form:

$$\sum_{p=1}^{125} k_p[a_p u_p^{*,\mathrm{num}} + (1-a_p)u_p^{**,\mathrm{num}}] = \bar{f}\,, \tag{9}$$

where $\bar{f} = 0$ in the case of zero source $f_l = 0$ in Eq. (1). The unknown stencil coefficients k_p ($p = 1, 2, \dots, 125$) are to be determined from the minimization of the local truncation error. The coefficients $a_p = 1$ if the grid point u_p belongs to material $*$ or $a_p = 0$ if the grid point u_p belongs to another material $**$. Only one variable $u_p^{*,\text{num}}$ or $u_p^{**,\text{num}}$ is actually included into Eq. (9) for each grid point. The coefficients a_p for Fig. 1b are: $a_p = 1$ ($p = 1, 2, \dots, 15, 19, 20, 25, \dots, 40, 44, 45, 50, \dots, 65, 69, 70, 76, \dots, 125$) and $a_p = 0$ ($p = 16, 17, 18, 21, \dots, 24, 41, 42, 43, 46, \dots, 49, 66, 67, 68, 71, \dots, 75$).

The local truncation error e follows from Eq. (9) by the replacement of the numerical solution $u_p^{*,\text{num}}$ and $u_p^{**,\text{num}}$ by the exact solution u_p^* and u_p^{**}:

$$e = \sum_{p=1}^{125} k_p[a_p u_p^* + (1 - a_p)u_p^{**}] - \bar{f}\,. \tag{10}$$

Next, we include the interface conditions for the exact solution at a small number N_G of the interface points into the expression for the local truncation error, Eq. (10), as additional constraints:

$$\begin{aligned} e = &\sum_{p=1}^{125} k_p[a_p u_p^* + (1 - a_p)u_p^{**}] + \{\sum_{j=1}^{N_G} q_{1,j}(u_{G,j}^* - u_{G,j}^{**} - \delta_{1,j}) \\ &+ \sum_{j=1}^{N_G} h q_{2,j}[c_*(n_{x,j}\frac{\partial u_{G,j}^*}{\partial x} + n_{y,j}\frac{\partial u_{G,j}^*}{\partial y} + n_{z,j}\frac{\partial u_{G,j}^*}{\partial z}) \\ &- c_{**}(n_{x,j}\frac{\partial u_{G,j}^{**}}{\partial x} + n_{y,j}\frac{\partial u_{G,j}^{**}}{\partial y} + n_{z,j}\frac{\partial u_{G,j}^{**}}{\partial z}) - \delta_{2,j}]\} - \bar{f}\,, \end{aligned} \tag{11}$$

where $n_{x,j}$, $n_{y,j}$ and $n_{z,j}$ are the x-, y-, and z-components of the normal vectors at the N_G selected interface points (see Fig. 1b), $\delta_{1,j}$ and $\delta_{2,j}$ are the given jumps for the function and fluxes at the N_G selected interface points, the coefficients $q_{1,j}$ and $q_{2,j}$ ($j = 1, 2, \dots, N_G$) are Lagrange multipliers. The expressions after the coefficients $q_{1,j}$ and $q_{2,j}$ are the interface conditions at the N_G selected interface points. Therefore, the expression in the curled brackets in Eq. (11) is zero (see Eq. (2)) and Eqs. (10) and (11) yield the same local truncation error e. The addition of the interface conditions at N_G points in Eq. (11) with the unknown coefficients $q_{1,j}$, $q_{2,j}$ ($j = 1, 2, \dots, N_G$) provides coupling between the unknown functions u_p^* and u_p^{**} used in the stencil equation, Eq. (9), and allows us to get a high accuracy of the proposed method for general geometry of interfaces.

Remark 2. Only $125+2N_G-1$ out of the $125+2N_G$ coefficients k_p, $q_{1,j}$, $q_{2,j}$ ($p = 1, 2, \dots, 125$, $j = 1, 2, \dots, N_G$) in Eq. (11) can be considered as unknown coefficients. This limitation can be explained as follows. In the case of zero jumps $\delta_1 = \delta_2 = 0$ (see Eq. (2) as well as Eq. (17) below), zero source $f_l = 0$ and $\bar{f} = 0$, Eq. (9) can be rescaled by the division of the left- and right-hand sides of Eq. (9) by any scalar, i.e., one of the coefficients k_p can be selected as unity and there will be only $125 + 2N_G - 1$ unknown rescaled coefficients. The case of nonzero term $\bar{f} \neq 0$ can be similarly treated because the term $\bar{f}$ is a linear function of the coefficients k_p, $q_{1,j}$, $q_{2,j}$ ($p = 1, 2, \dots, 125$; $j = 1, 2, \dots, N_G$); see below. For convenience, we will scale the stencil coefficients in such a way that k_{63} is $k_{63} = 1$.

For the minimization of the local truncation error e, we first expand it into a Taylor series. In order to do this expansion, let us expand the exact solution at the grid points and at the N_G selected interface points in Eq. (11) into a Taylor series at small $h \ll 1$ in the vicinity of the central interface point G for the 125-point stencils as follows:

$$\begin{aligned} v_p = &v_G + \frac{\partial v_G}{\partial x}[(r_{x,p} - dx_G)h] + \frac{\partial v_G}{\partial y}[(r_{y,p} - dy_G)b_y h] + \frac{\partial v_G}{\partial z}[(r_{z,p} - dz_G)b_z h] \\ &+ \frac{\partial^2 v_G}{\partial x^2}\frac{[(r_{x,p} - dx_G)h]^2}{2!} + \frac{\partial^2 v_G}{\partial y^2}\frac{[(r_{y,p} - dy_G)b_y h]^2}{2!} + \frac{\partial^2 v_G}{\partial z^2}\frac{[(r_{z,p} - dz_G)b_z h]^2}{2!} \\ &+ 2\frac{\partial^2 v_G}{\partial x \partial y}\frac{[(r_{x,p} - dx_G)h][(r_{y,p} - dy_G)b_y h]}{2!} + \cdots, \quad p = 25(t-1) + 5(j-1) + i \\ &\text{with } i, j, t = 1, 2, 3, 4, 5 \end{aligned} \tag{12}$$

with $dx_G = \frac{x_G - x_{63}}{h}$, $dy_G = \frac{y_G - y_{63}}{b_y h}$, and $dz_G = \frac{z_G - z_{63}}{b_z h}$, and

$$w_j = w_G + \frac{\partial w_G}{\partial x}[d_{x,j}h] + \frac{\partial w_G}{\partial y}[d_{y,j}b_y h] + \frac{\partial w_G}{\partial z}[d_{z,j}b_z h] + \frac{\partial^2 w_G}{\partial x^2}\frac{[d_{x,j}h]^2}{2!} + \frac{\partial^2 w_G}{\partial y^2}\frac{[d_{y,j}b_y h]^2}{2!} + \frac{\partial^2 w_G}{\partial z^2}\frac{[d_{z,j}b_z h]^2}{2!} + 2\frac{\partial^2 w_G}{\partial x \partial y}\frac{[d_{x,j}h][d_{y,j}b_y h]}{2!} + \cdots . \qquad j = 1, 2, \ldots, N_G \tag{13}$$

In Eq. (12) the function v_p is u_p^*, u_p^{**}, in Eq. (13) the function w_j is $u_{G,j}^*$, $u_{G,j}^{**}$, $\frac{\partial u_{G,j}^*}{\partial x}$, $\frac{\partial u_{G,j}^{**}}{\partial x}$, $\frac{\partial u_{G,j}^*}{\partial y}$, $\frac{\partial u_{G,j}^{**}}{\partial y}$, $\frac{\partial u_{G,j}^*}{\partial z}$, $\frac{\partial u_{G,j}^{**}}{\partial z}$, the coefficients $d_{x,j}$, $d_{y,j}$, and $d_{z,j}$ are defined in Eq. (8) and $N_G = 81$. The exact solution u_G^* and u_G^{**} to the Poisson equations, Eq. (1), at the central interface point $x = x_G$, $y = y_G$ and $z = z_G$ meets the following equations:

$$\frac{\partial^2 u_G^*}{\partial x^2} = -\frac{\partial^2 u_G^*}{\partial y^2} - \frac{\partial^2 u_G^*}{\partial z^2} + \frac{1}{c_*} f^*, \qquad \frac{\partial^2 u_G^{**}}{\partial x^2} = -\frac{\partial^2 u_G^{**}}{\partial y^2} - \frac{\partial^2 u_G^{**}}{\partial z^2} + \frac{1}{c_{**}} f^{**}, \tag{14}$$

$$\frac{\partial^{(i+j+t+2)} u_G^*}{\partial z^t \partial y^i \partial x^{(2+j)}} = -\frac{\partial^{(i+j+t+2)} u_G^*}{\partial z^t \partial y^{(i+2)} \partial x^j} - \frac{\partial^{(i+j+t+2)} u_G^*}{\partial z^{(t+2)} \partial y^i \partial x^j} + \frac{1}{c_*}\frac{\partial^{(i+j+t)} f^*}{\partial z^t \partial y^i \partial x^j},$$
$$\frac{\partial^{(i+j+t+2)} u_G^{**}}{\partial z^t \partial y^i \partial x^{(2+j)}} = -\frac{\partial^{(i+j+t+2)} u_G^{**}}{\partial z^t \partial y^{(i+2)} \partial x^j} - \frac{\partial^{(i+j+t+2)} u_G^{**}}{\partial z^{(t+2)} \partial y^i \partial x^j} + \frac{1}{c_{**}}\frac{\partial^{(i+j+t)} f^{**}}{\partial z^t \partial y^i \partial x^j} \tag{15}$$

with $i, j, t = 0, 1, 2, 3, 4, \ldots$. Eq. (15) is obtained by the differentiation of Eq. (14) with respect to x, y and z. Inserting Eqs. (12)–(15) with zero source term $f^* = f^{**} = 0$ into Eq. (11) we get the following local truncation error in space e:

$$\begin{aligned}
e = {} & b_1 u_G^* + b_2 u_G^{**} + h(b_3\frac{\partial u_G^*}{\partial z} + b_4\frac{\partial u_G^{**}}{\partial z} + b_5\frac{\partial u_G^*}{\partial y} + b_6\frac{\partial u_G^{**}}{\partial y} + b_7\frac{\partial u_G^*}{\partial x} + b_8\frac{\partial u_G^{**}}{\partial x}) \\
& + h^2(b_9\frac{\partial^2 u_G^*}{\partial z^2} + b_{10}\frac{\partial^2 u_G^{**}}{\partial z^2} + b_{11}\frac{\partial^3 u_G^*}{\partial z \partial y^2} + b_{12}\frac{\partial^3 u_G^{**}}{\partial z \partial y^2} + b_{13}\frac{\partial^2 u_G^*}{\partial y^2} + b_{14}\frac{\partial^2 u_G^{**}}{\partial y^2} + b_{15}\frac{\partial^3 u_G^*}{\partial z \partial x^2} + b_{16}\frac{\partial^3 u_G^{**}}{\partial z \partial x^2} \\
& + b_{17}\frac{\partial^2 u_G^*}{\partial x \partial y} + b_{18}\frac{\partial^2 u_G^{**}}{\partial x \partial y}) \\
& + h^3(b_{19}\frac{\partial^3 u_G^*}{\partial z^3} + b_{20}\frac{\partial^3 u_G^{**}}{\partial z^3} + b_{21}\frac{\partial^3 u_G^*}{\partial z^2 \partial y} + b_{22}\frac{\partial^3 u_G^{**}}{\partial z^2 \partial y} + b_{23}\frac{\partial^3 u_G^*}{\partial z \partial y^2} + b_{24}\frac{\partial^3 u_G^{**}}{\partial z \partial y^2} b_{25}\frac{\partial^3 u_G^*}{\partial y^3} \\
& + b_{26}\frac{\partial^3 u_G^{**}}{\partial y^3} + b_{27}\frac{\partial^3 u_G^*}{\partial z^2 \partial x} + b_{28}\frac{\partial^3 u_G^{**}}{\partial z^2 \partial x} + b_{29}\frac{\partial^3 u_G^*}{\partial z \partial y \partial x} + b_{30}\frac{\partial^3 u_G^{**}}{\partial z \partial y \partial x} + b_{31}\frac{\partial^3 u_G^*}{\partial x \partial y^2} + b_{32}\frac{\partial^3 u_G^{**}}{\partial x \partial y^2}) \\
& + h^4(b_{33}\frac{\partial^4 u_G^*}{\partial z^4} + \cdots + b_{50}\frac{\partial^4 u_G^{**}}{\partial x \partial y^3}) + h^5(b_{51}\frac{\partial^5 u_G^*}{\partial z^5} + \cdots + b_{72}\frac{\partial^5 u_G^{**}}{\partial x \partial y^4}) + h^6(b_{73}\frac{\partial^6 u_G^*}{\partial z^6} + \cdots + b_{98}\frac{\partial^6 u_G^{**}}{\partial x \partial y^5}) \\
& + h^7(b_{99}\frac{\partial^7 u_G^*}{\partial z^7} + \cdots + b_{128}\frac{\partial^7 u_G^{**}}{\partial x \partial y^6}) \\
& + h^8(b_{129}\frac{\partial^8 u_G^*}{\partial z^8} + \cdots + b_{162}\frac{\partial^8 u_G^{**}}{\partial x \partial y^7}) + h^9(b_{163}\frac{\partial^9 u_G^*}{\partial z^9} + \cdots + b_{200}\frac{\partial^9 u_G^{**}}{\partial x \partial y^8}) + h^{10}(b_{201}\frac{\partial^{10} u_G^*}{\partial z^{10}} + \cdots \\
& + b_{242}\frac{\partial^{10} u_G^{**}}{\partial x \partial y^9}) + h^{11}(b_{243}\frac{\partial^{11} u_G^*}{\partial z^{11}} + \cdots + b_{288}\frac{\partial^{11} u_G^{**}}{\partial x \partial y^{10}}) \\
& + h^{12}(b_{289}\frac{\partial^{12} u_G^*}{\partial z^{12}} + \cdots + b_{338}\frac{\partial^{12} u_G^{**}}{\partial x \partial y^{11}}) + h^{13}(b_{339}\frac{\partial^{13} u_G^*}{\partial z^{13}} + \cdots + b_{392}\frac{\partial^{13} u_G^{**}}{\partial x \partial y^{12}}) \\
& + h^{14}(b_{393}\frac{\partial^{14} u_G^*}{\partial z^{14}} + \cdots + b_{450}\frac{\partial^{14} u_G^{**}}{\partial x \partial y^{13}})
\end{aligned}$$

$$+h^{15}(b_{451}\frac{\partial^{15}u_G^*}{\partial z^{15}}+\cdots+b_{512}\frac{\partial^{15}u_G^{**}}{\partial x\partial y^{14}})+h^{16}(b_{513}\frac{\partial^{16}u_G^*}{\partial z^{16}}+\cdots+b_{578}\frac{\partial^{16}u_G^{**}}{\partial x\partial y^{15}})$$

$$-[\bar{f}+\sum_{j=1}^{N_G}(q_{1,j}\delta_{1,j}+hq_{2,j}\delta_{2,j})]+O(h^7)$$

$$=e_b-[\bar{f}+\sum_{j=1}^{N_G}(q_{1,j}\delta_{1,j}+hq_{2,j}\delta_{2,j})]+O(h^7) \tag{16}$$

where the coefficients b_p ($p=1,2,\ldots$) are expressed in terms of the coefficients k_i and $q_{1,j}$, $q_{2,j}$ ($i=1,2,\ldots,125$, $j=1,2,\ldots,N_G$) and are given in Appendix A, the term e_b includes only the sum of all terms with the coefficients b_p in the expression for the local truncation error (compare the expressions after the first and second equalities in Eq. (16)). The expression for the local truncation error, Eq. (16), includes only the first order derivatives with respect to x (the higher order derivatives with respect to x are excluded with the help of Eqs. (14)–(15)). Zeroing the last expression in the square brackets in Eq. (16), we can find the right-hand side of the stencil equation $\bar{f}$ due to the given jumps δ_1 and δ_2:

$$\bar{f}=-\sum_{j=1}^{N_G}(q_{1,j}\delta_{1,j}+hq_{2,j}\delta_{2,j})\,. \tag{17}$$

Due to Eq. (17), the local truncation error e in Eq. (16) is independent of the right-hand side of the stencil equation $\bar{f}$ and the jumps δ_1 and δ_2 as well as $e=e_b$.

3.1.1. Homogeneous materials (without interface)

For homogeneous materials all a_p ($p=1,2,\ldots,125$) coefficients are $a_j=1$ (see Eq. (9) if we consider material $*$) as well as all $q_{1,j}=q_{2,j}=0$ ($j=1,2,\ldots,N_G$) are zero. In this case the derivation of the local truncation error is similar to that in the previous section with $b_p=0$ (p = 2,4,6,8, ...) in Eq. (16) if we consider material $*$. The unknown stencil coefficients k_i ($i=1,2,\ldots,125$) can be found by zeroing the coefficients $b_p=0$ (p = 1,3,5, ...) in Eq. (16) with the smallest numbers of index p. Symbolic computations with Mathematica show that after zeroing the first 144 coefficients $b_p=0$ (p = 1,3,5, ..., 287) for rectangular meshes ($b_y\neq 1$ and/or $b_z\neq 1$), at least one of the coefficients b_p ($289\leq p\leq 338$) is always non-zero, i.e., the maximum possible order of the local truncation error is 12 for rectangular meshes. Similarly, after zeroing the first 256 coefficients $b_p=0$ ($p=1,3,5,\ldots,511$) for square meshes ($b_y=b_z=1$), at least one of the coefficients b_p ($513\leq p\leq 578$) is always non-zero, i.e., the maximum possible order of the local truncation error is 16 for square meshes and it is 4 orders higher than that for rectangular meshes. Symbolic computations also show that in order to have 125 algebraic equations for finding 125 stencil coefficients k_i for square meshes, we should also zero some of coefficients b_p ($513\leq p\leq 578$) corresponding to the 16th order with respect to h in Eq. (16). However, we can significantly simplify the calculations by zeroing the stencil coefficients $k_{13}=k_{53}=k_{61}=k_{65}=k_{73}=k_{113}=0$ corresponding to the grid points located at the centers of the six faces of the 125-point cell. This simplification does not change the maximum possible order of the local truncation error but this allows us to avoid the use of a very large number of the long expressions of the coefficients b_p ($451\leq p\leq 578$) corresponding to the 15th and 16th orders with respect to h in Eq. (16).

For square meshes the stencils coefficients k_i ($i=1,2,\ldots,125$) with $k_{63}=1$ and $k_{13}=k_{53}=k_{61}=k_{65}=k_{73}=k_{113}=0$ can be analytically found by zeroing the first 225 coefficients $b_p=0$ ($p=1,3,5,\ldots,449$) up to the 14th order with respect to h (the Mathematica program can select just linearly independent algebraic equations from this system). These coefficients k_i ($i=1,2,\ldots,125$) are:

$$k_1=-\frac{3645}{477569996}\,,\qquad k_2=-\frac{96173}{2149064982}\,,\qquad k_3=-\frac{194003}{4298129964}\,,\ldots \tag{18}$$

(see the attached file k-coeff-cubic.nb for the all stencil coefficients k_i, $i = 1, 2, \ldots, 125$) with the following local truncation error:

$$e = \frac{h^{16}}{900729869271724800}[-536345375\frac{\partial^{16}u_{63}}{\partial z^{16}} - 2145381500\frac{\partial^{16}u_{63}}{\partial y^2\partial z^{14}} - 4534176182\frac{\partial^{16}u_{63}}{\partial y^4\partial z^{12}} - 6093693296\frac{\partial^{16}u_{63}}{\partial y^6\partial z^{10}} - 6873451853\frac{\partial^{16}u_{63}}{\partial y^8\partial z^8} - 6093693296\frac{\partial^{16}u_{63}}{\partial y^{10}\partial z^6} - 4534176182\frac{\partial^{16}u_{63}}{\partial y^{12}\partial z^4} - 2145381500\frac{\partial^{16}u_{63}}{\partial y^{14}\partial z^2} - 536345375\frac{\partial^{16}u_{63}}{\partial y^{16}}] + O(h^{18}). \tag{19}$$

As can be seen from Eq. (19), for homogeneous materials and square ($b_y = b_z = 1$) Cartesian meshes, the stencil coefficients k_i ($i = 1, 2, \ldots, 125$) provide the 16th order of the local truncation error. It can be also shown that on rectangular ($b_y \neq b_z \neq 1$) Cartesian meshes, OLTEM with the 125-point stencils provides the 12th order of the local truncation error. Note that in the 2-D case OLTEM with the $5 \times 5 = 25$-point stencils (similar to those for quadratic finite elements) provides 16th and 20th orders of the local truncation error on the rectangular and square ($b_y = 1$) Cartesian meshes, respectively (see our paper [30]). These results mean that the maximum possible orders of accuracy of OLTEM with the $5 \times 5 = 25$-point stencils in the 2-D case and the $5 \times 5 \times 5 = 125$-point stencils in the 3-D case are different, i.e., we have a special superconvergent case of OLTEM for the Poisson equation with homogeneous materials in the 2-D case. We have not observed different orders of convergence of OLTEM in the 2-D and 3-D cases with similar stencils (having the same number of points along the Cartesian axes) for other PDEs such as the time-independent elasticity equations as well as the time-dependent scalar wave and heat transfer equations and elastodynamics equations, e.g., see our paper [35].

3.1.2. Heterogeneous materials with an irregular interface

In our paper [31] on OLTEM for the 2-D Poisson equation with irregular interfaces we showed that the maximum possible order of the local truncation error for heterogeneous 25-point stencils is 12. In order to get the same order of the local truncation error for the heterogeneous 125-point stencil in the 3-D case considered here, we will use the following procedure.

We use the 280 unknown stencil coefficients k_i ($i = 1, 2, \ldots, 125$ with $k_{63} = 1$ as well as $k_{13} = k_{53} = k_{61} = k_{65} = k_{73} = k_{113} = 0$; see Section 3.1.1), and $q_{1,j}$, $q_{2,j}$ ($j = 1, 2, \ldots, 81$) in order to minimize the local truncation error. Symbolic computations with Mathematica for homogeneous materials show that starting from the ninth order with respect to h in Eq. (16), some of the coefficients b_p are linearly dependent. Therefore, we zero the first 200 coefficients b_p in Eq. (16) up to the ninth order with respect to h, i.e.,

$$b_p = 0, \qquad p = 1, 2, \ldots, 200. \tag{20}$$

Then, in order to have a sufficient number of equations for the calculation of the 280 unknown stencil coefficients k_i and $q_{1,j}$, $q_{2,j}$, we use the least square method for the minimization of coefficients b_p related to the 10th, 11th, 12th, 13th and 14th, orders of the local truncation error with the following residual R:

$$R = \sum_{p=201}^{242} b_p^2 + h_1 \sum_{p=243}^{288} b_p^2 + h_2 \sum_{p=289}^{338} b_p^2 + h_3 \sum_{p=339}^{392} b_p^2 + h_4 \sum_{p=393}^{450} b_p^2, \tag{21}$$

where h_1, h_2, h_3 and h_4 are the weighting factors to be selected (e.g., the numerical experiments show that $h_1 = 0.2$, $h_2 = 0.2h_1$, $h_3 = h_4 = 0.2h_2$ yields accurate results).

In order to minimize the residual R with the constraints given by Eq. (20), we can form a new residual $\bar{R}$ with the Lagrange multipliers λ_l:

$$\bar{R} = \sum_{l=1}^{200} \lambda_l b_l + \sum_{p=201}^{242} b_p^2 + h_1 \sum_{p=243}^{288} b_p^2 + h_2 \sum_{p=289}^{338} b_p^2 + h_3 \sum_{p=339}^{392} b_p^2 + h_4 \sum_{p=393}^{450} b_p^2. \tag{22}$$

The residual $\bar{R}$ is a quadratic function of the stencil coefficients k_i ($i = 1, 2, \ldots, 125$) and $q_{1,j}$, $q_{2,j}$ ($j = 1, 2, \ldots, 81$) and a linear function of the Lagrange multipliers λ_l, i.e., $\bar{R} = \bar{R}(k_i, q_{1,j}, q_{2,j}, \lambda_l)$. In order minimize

the residual $\bar{R} = \bar{R}(k_i, q_{1,j}, q_{2,j}, \lambda_l)$, the necessary conditions are given by:

$$\frac{\partial \bar{R}}{\partial k_i} = 0\,, \qquad \frac{\partial \bar{R}}{\partial q_{1,j}} = 0\,, \qquad \frac{\partial \bar{R}}{\partial q_{2,j}} = 0\,, \qquad \frac{\partial \bar{R}}{\partial \lambda_l} = 0\,, \tag{23}$$
$$i = 1, 2, \ldots, 125\,, \qquad j = 1, 2, \ldots, 81\,, \qquad l = 1, 2, \ldots, 200\,,$$

where equation $\frac{\partial \bar{R}}{\partial k_i} = 0$ ($i = 63, 13, 53, 61, 65, 73, 113$) in Eq. (23) should be replaced by $k_{63} = 1$ and $k_{13} = k_{53} = k_{61} = k_{65} = k_{73} = k_{113} = 0$ (see Remark 2). Eq. (23) forms a system of 487 linear algebraic equations with respect to 287 coefficients k_i ($i = 1, 2, \ldots, 125$) and $q_{1,j}$, $q_{2,j}$($j = 1, 2, \ldots, 81$) as well as 200 Lagrange multipliers λ_l ($l = 1, 2, \ldots, 200$). Solving these linear algebraic equations numerically, we can find the coefficients k_i ($i = 1, 2, \ldots, 125$) for the 125-point uniform stencils as well as $q_{1,j}$, $q_{2,j}$ ($j = 1, 2, \ldots, 81$). The presented procedure provides the 12th order of the local truncation error for the 125-point uniform stencils with the general geometry of the interface. As can be seen from the above procedure, we use the coefficients k_i ($i = 1, 2, \ldots, 125$) and $q_{1,j}$, $q_{2,j}$ ($j = 1, 2, \ldots, N_G$ with $N_G = 81$) in order to zero and minimize the coefficients b_p in Eqs. (20)–(23). At a small number N_G of the interface points, we do not have a sufficient of number of the coefficients $q_{1,j}$, $q_{2,j}$ ($j = 1, 2, \ldots, N_G$) for the minimization of the coefficients b_p and cannot obtain a very high accuracy. Similar to the 2-D case with $N_G = 9$ (see our paper [31]), in the 3-D case we select $N_G = 9 \times 9 = 81$ interface points and obtain the 12th order of the local truncation error similar to that in the 2-D case. The 125-point uniform stencils of OLTEM for a homogeneous material (without interface) provide the 16th order of the local truncation error for square meshes (see Eq. (19)). In this case the global error is defined by the order of accuracy of the 125-point stencils with interfaces. This accuracy of the OLTEM stencils leads to the 11th order of accuracy of global solutions (see the numerical examples below). Moreover, the new approach also minimizes the leading high-order terms b_p of the local truncation error in Eq. (22).

Remark 3. We should mention that the representation of the coefficients b_i in Eq. (16) as $b_i = \sum_{j=1}^{125} s_{ij} k_j + \sum_{j=1}^{81} (c_{ij}^1 q_{1,j} + c_{ij}^2 q_{2,j})\,, i = 1, 2, \ldots, 578$ as well as the explicit analytical formulas for $\frac{\partial \bar{R}}{\partial k_i}$, $\frac{\partial \bar{R}}{\partial q_{1,j}}$, $\frac{\partial \bar{R}}{\partial q_{2,j}}$, $\frac{\partial \bar{R}}{\partial \lambda_l}$ (see Eq. (23)) in terms of the coefficients s_{ij}, c_{ij}^1 and c_{ij}^2 (see Appendix B) significantly simplify the derivation of the local system of algebraic equations for finding the stencil coefficients k_i ($i = 1, 2, \ldots, 125$) allowing us to extend our approach to the 3-D case.

The global discrete system of equations includes the 125-point stencils for homogeneous materials without interfaces and the 125-point stencils for heterogeneous materials with interfaces between different materials (see Fig. 1) for all internal grid points located inside the domain. The global system of equations for OLTEM has the non-symmetric stiffness matrix and can be solved with an iterative solver (e.g., we use the built-in Matlab solver 'gmres' [36] without preconditioners). The new approach does not use unknowns at the interfaces, and the global discrete system of equations has the same unknowns for homogeneous and heterogeneous materials (the same structures of the sparse global matrices, the difference is only in the values of the stencil coefficients k_p (see Eq. (9)) of the global matrices for homogeneous and heterogeneous materials).

Remark 4. To estimate the computation costs of the formation and solution of 487 linear algebraic equations given by Eq. (23), we formed and solved 10^4 such systems with a general Matlab solver [36] on a desktop computer (Processor: Intel (R) Core(TN) i9-9900 CPU @3.10 Hz 3.10 Hz). The computation 'wall' time was $T = 200$ s for 10^3 systems, or the average time for one system was 0.2 s. Because the coefficients k_p are independently calculated for different stencils, the computation time of their calculation for different stencils can be significantly reduced on parallel computers. These local systems are numerically solved only for the grid points located close to the interface (for heterogeneous stencils). For the stencils with homogeneous materials, the stencil coefficients are analytically defined; see Eq. (18). Therefore, for large global systems of equations, the computation time for the calculation of the coefficients k_p is very small compared to that for the solution of the global system of algebraic equations. Note that the coefficients $q_{1,j}$, $q_{2,j}$ calculated from the local system of equations, Eq. (23), are only used for the calculation of non-zero right-hand side vector (see below Section 3.2) while the Lagrange multipliers λ_l in the local system of equations, Eq. (23), are not used in the global system of equations at all. We should also mention that for variable material properties (not considered in the paper), the stencil coefficients should be calculated for each internal grid point. In this case the computation time for the calculation of the stencil coefficients for all stencils will be proportional to the number of internal grid points.

Remark 5. The stencil coefficients can be also derived using the Taylor series expansion about the central grid point with the coordinates x_{63}, y_{63} and z_{63} instead of the interface point with the coordinates x_G, y_G and z_G.

3.2. Nonzero source term $f_l \neq 0$

The inclusion of non-zero source term f_l in the partial differential equation, Eq. (1), leads to the additional contribution to the term $\bar{f}$ in the stencil equation, Eq. (9). The functions f_l can be discontinuous across the interfaces. The expression for the term $\bar{f}$ can be calculated from the procedure used for the derivation of the local truncation error in the case of zero source term as follows. In the case of non-zero source term $f_l(\boldsymbol{x}) \neq 0$, the insertion of Eqs. (12)–(15) into Eq. (11) yields the following local truncation error in space e_f:

$$e_f = e_b - [\bar{f} + \sum_{j=1}^{81}(q_{1,j}\delta_{1,j} + hq_{2,j}\delta_{2,j}) - \mathbf{h}^2\{\sum_{j=1}^{125}\frac{1}{2}(r_{x,j} - dx_G)(a_j\tilde{f}_G^* + (1-a_j)\tilde{f}_G^{**})k_j + \sum_{j=1}^{81}[\frac{1}{2}d_{x,j}^2(\tilde{f}_G^* - \tilde{f}_G^{**})q_{1,j} + d_{x,j}n_{x,j}(c_*\tilde{f}_G^* - c_{**}\tilde{f}_G^{**})q_{2,j}]\} - \mathbf{h}^3...], \tag{24}$$

where e_b is the local truncation error in space given by Eq. (16) for zero source term, $\tilde{f}_G^*$ and $\tilde{f}_G^{**}$ designate functions $\frac{f^*(x,y,z)}{c_*}$ and $\frac{f^{**}(x,y,z)}{c_{**}}$ calculated at the interface point with the coordinates $x = x_G$, $y = y_G$ and $z = z_G$.

Equating to zero the expression in the square brackets in the right-hand side of Eq. (24), we will get the expression for $\bar{f}$:

$$\begin{aligned}\bar{f} &= -\sum_{j=1}^{81}(q_{1,j}\delta_{1,j} + hq_{2,j}\delta_{2,j}) + \sum_{j=1}^{125}\hat{f}_j^1 k_j + \sum_{j=1}^{81}(\hat{f}_j^2 q_{1,j} + \hat{f}_j^3 q_{2,j}) \\ &= -\sum_{j=1}^{81}(q_{1,j}\delta_{1,j} + hq_{2,j}\delta_{2,j}) + \mathbf{h}^2\{\sum_{j=1}^{125}\frac{1}{2}(r_{x,j} - dx_G)(a_j\tilde{f}_G^* + (1-a_j)\tilde{f}_G^{**})k_j + \sum_{j=1}^{81}[\frac{1}{2}d_{x,j}^2(\tilde{f}_G^* - \tilde{f}_G^{**})q_{1,j} \\ &\quad + d_{x,j}n_{x,j}(c_*\tilde{f}_G^* - c_{**}\tilde{f}_G^{**})q_{2,j}]\} + \mathbf{h}^3...,\end{aligned} \tag{25}$$

as well as we will get the same local truncation errors $e_f = e_b$ for zero and non-zero source term. The coefficients $\hat{f}_j^1$ $(j = 1, 2, \ldots, 125)$, $\hat{f}_j^2$ and $\hat{f}_j^3 (j = 1, 2, \ldots, 81)$ in Eq. (25) are:

$$\begin{aligned}\hat{f}_j^1 &= \mathbf{h}^2(\frac{1}{2}(r_{x,j} - dx_G)(a_j\tilde{f}_G^* + (1-a_j)\tilde{f}_G^{**})) + \mathbf{h}^3..., \\ \hat{f}_j^2 &= \mathbf{h}^2(\frac{1}{2}d_{x,j}^2(\tilde{f}_G^* - \tilde{f}_G^{**})) + \mathbf{h}^3..., \qquad \hat{f}_j^3 = \mathbf{h}^2 d_{x,j}n_{x,j}(c_*\tilde{f}_G^* - c_{**}\tilde{f}_G^{**}) + \mathbf{h}^3...,\end{aligned} \tag{26}$$

see the attached file RHS.nb for the detailed expressions of $\hat{f}_j^1$, $\hat{f}_j^2$ and $\hat{f}_j^3$. This procedure means that the coefficients k_i $(i = 1, 2, \ldots, 125)$ of the stencil equations are first calculated for zero source term $f_l = 0$ as described in Section 3.1. Then, the nonzero source term $\bar{f}$ given by Eq. (25) is used in the stencil equation, Eq. (9).

4. OLTEM for post-processing of numerical results — calculations of spatial derivatives

For the analysis of engineering problems the calculations of the spatial derivatives of primary functions are necessary in many cases, e.g., the spatial derivatives of function u_l in Eq. (1). Therefore, after the calculation of the numerical solution for the primary functions, many computer codes include special post-processing procedures for the calculation of the spatial derivatives of the numerical solution for the primary functions. Here we show the application of OLTEM with the 125-point stencils (the same as we used in the previous section; see also Fig. 1) for the calculation of $\frac{\partial u^{\text{num}}}{\partial x}$, $\frac{\partial u^{\text{num}}}{\partial y}$ and $\frac{\partial u^{\text{num}}}{\partial z}$. Because the calculations of these three derivatives are similar then we show the procedure in detail for $\frac{\partial u^{\text{num}}}{\partial x}$.

The 125-point stencils for the calculation of $\frac{\partial u^{\text{num}}}{\partial x}$ at the central stencil point with the coordinates x_{63}, y_{63} and z_{63} (see Fig. 1) can be selected similar to Eq. (9) as follows:

$$-[a_{63}\frac{\partial u_{63}^{*,\text{num}}}{\partial x} + (1-a_{63})\frac{\partial u_{63}^{**,\text{num}}}{\partial x}]h + \sum_{p=1}^{125}k_p[a_p u_p^{*,\text{num}} + (1-a_p)u_p^{**,\text{num}}] = \bar{f}, \tag{27}$$

where $a_{63} = 1$ if the central stencil point belongs to material $*$ and $a_{63} = 0$ if the central stencil point belongs to material $**$. The local truncation error e_p for Eq. (27) can be obtained by the replacement of the numerical solution $u_p^{*,\text{num}}$ and $u_p^{**,\text{num}}$ in Eq. (27) by the exact solution u_p^* and u_p^{**}:

$$e_p = -[a_{63}\frac{\partial u_{63}^*}{\partial x} + (1-a_{63})\frac{\partial u_{63}^{**}}{\partial x}]h + \sum_{p=1}^{125} k_p[a_p u_p^* + (1-a_p)u_p^{**}] - \bar{f}\,. \tag{28}$$

Similar to Eq. (11) in Section 3, we include the interface conditions for the exact solution at the same small number N_G of the interface points into the expression for the local truncation error in Eq. (28) as constraints:

$$\begin{aligned} e_p = &-[a_{63}\frac{\partial u_{63}^*}{\partial x} + (1-a_{63})\frac{\partial u_{63}^{**}}{\partial x}]h + \sum_{p=1}^{125} k_p[a_p u_p^* + (1-a_p)u_p^{**}] + \{\sum_{j=1}^{N_G} q_{1,j}(u_{G,j}^* - u_{G,j}^{**} - \delta_{1,j}) \\ &+ \sum_{j=1}^{N_G} hq_{2,j}[c_*(n_{x,j}\frac{\partial u_{G,j}^*}{\partial x} + n_{y,j}\frac{\partial u_{G,j}^*}{\partial y} + n_{z,j}\frac{\partial u_{G,j}^*}{\partial z}) \\ &- c_{**}(n_{x,j}\frac{\partial u_{G,j}^{**}}{\partial x} + n_{y,j}\frac{\partial u_{G,j}^{**}}{\partial y} + n_{z,j}\frac{\partial u_{G,j}^{**}}{\partial z}) - \delta_{2,j}]\} - \bar{f}\,, \end{aligned} \tag{29}$$

(see the corresponding explanations in Section 3.1). Similar to Section 3, first we consider the case of zero source term $f_l = \bar{f} = 0$. For the accurate calculation of the derivative $\frac{\partial u^{\text{num}}}{\partial x}$, we should minimize the local truncation error e_p in Eq. (29). Repeating the procedure described in Section 3.1 and using Eqs. (12)–(15) with zero source term $f^* = f^{**} = 0$ we will also get the local truncation error in space e_p given by Eq. (16) with the coefficients b_p $(p = 1, 2, \ldots)$ expressed in terms of the coefficients k_i and $q_{1,j}$, $q_{2,j}$ $(i = 1, 2, \ldots, 125,\ j = 1, 2, \ldots, N_G)$ and given in the file b-coef-post.nb'(these coefficients b_p $(p = 1, 2, \ldots)$ are slightly different from those used in basic computations in the previous Section 3).

For homogeneous materials (without interfaces), the coefficients $q_{1,j} = q_{2,j} = 0$ $(j = 1, 2, \ldots, N_G)$ are zero and the stencils coefficients k_i $(i = 1, 2, \ldots, 125)$ can be analyzed and calculated similar to those in Section 3.1.1. Symbolic computations with Mathematica show that in the case of post-processing, after zeroing the first 121 coefficients $b_p = 0$ $(p = 1, 3, 5, \ldots, 242)$, at least one of the coefficients b_p $(289 \le p \le 338)$ is always non-zero for rectangular and square meshes, i.e., the maximum possible order of the local truncation error is 11. Symbolic computations also show that in order to have 125 algebraic equations for finding 125 stencil coefficients k_i for square meshes, we should also zero some of coefficients b_p $(513 \le p \le 578)$ corresponding to the 16th order with respect to h in Eq. (16). However, we can significantly simplify the calculations by zeroing the stencil coefficients $k_{63} = k_{13} = k_{53} = k_{61} = k_{65} = k_{73} = k_{113} = 0$ corresponding to the grid point located at the center of the 125-point cell as well as to the grid points located at the centers of the six faces of the 125-point cell. This simplification does not change the maximum possible order of the local truncation error but allows us to avoid the use of a very large number of the long expressions for the coefficients b_p $(451 \le p \le 578)$ corresponding to the 15th and 16th orders with respect to h in Eq. (16).

For square meshes and homogeneous materials, the stencils coefficients k_i $(i = 1, 2, \ldots, 125)$ with $k_{63} = k_{13} = k_{53} = k_{61} = k_{65} = k_{73} = k_{113} = 0$ can be analytically found by zeroing the following coefficients $b_p = 0$ (p = 1,3,5, …, 377, 389, 391, 393, 395, 397) (the Mathematica program can select just linearly independent algebraic equations from this system) that do not include the coefficients b_p $(p > 450)$ corresponding to the 15th order and higher orders with respect to h. These coefficients k_i $(i = 1, 2, \ldots, 125)$ are:

$$k_1 = -\frac{221}{630000}\,, \qquad k_2 = -\frac{727}{770000}\,, \qquad k_3 = 0\,, \ldots \tag{30}$$

(see the attached file k-coeff-cubic-post.nb for the all stencil coefficients k_i, $i = 1, 2, \ldots, 125$). They provide the following local truncation error, Eq. (29):

$$e_p = -\frac{h^{11}}{519750}[\frac{\partial^{11} u_{63}}{\partial x \partial y^6 \partial z^4} + \frac{\partial^{11} u_{63}}{\partial x \partial y^8 \partial z^2} + \frac{\partial^{11} u_{63}}{\partial x \partial y^{10}}] + O(h^{12})\,. \tag{31}$$

For heterogeneous materials with interfaces, the stencil coefficients k_i and $q_{1,j}$, $q_{2,j}$ $(i = 1, 2, \ldots, 125,\ j = 1, 2, \ldots, N_G)$ are calculated similar to those in Section 3.1.2 from 487 linear algebraic equations formed

by Eq. (23) where equation $\frac{\partial \bar{R}}{\partial k_i} = 0$ ($i = 63, 13, 53, 61, 65, 73, 113$) in Eq. (23) should be replaced by $k_{63} = k_{13} = k_{53} = k_{61} = k_{65} = k_{73} = k_{113} = 0$. Similar to homogeneous materials, the stencil coefficients for heterogeneous materials provide the 11th order of accuracy for the local truncation error e_p.

The case of nonzero source term $f_l \neq 0$ is treated similar to that in Section 3.2. The final expression for the term $\bar{f}$ in Eq. (27) is also described by Eq. (25); see the attached file RHS-post.nb for the detailed expressions of $\hat{f}_j^1$, $\hat{f}_j^2$ and $\hat{f}_j^3$.

To summarize, for the calculation of the derivative $\frac{\partial u^{\text{num}}}{\partial x}$ using OLTEM with the 125-point stencils, we follow the following procedure:

- Calculate the stencil coefficients k_i and $q_{1,j}$, $q_{2,j}$ ($i = 1, 2, \ldots, 125$, $j = 1, 2, \ldots, N_G$) for each internal grid point as described above in Section 4 for homogeneous (without interfaces) and heterogeneous (with interfaces) materials.
- Using these stencil coefficients, calculate the right-hand side $\bar{f}$ in Eq. (27) for each internal grid point using Eq. (25).
- Calculate the derivative $\frac{\partial u^{\text{num}}}{\partial x}$ from Eq. (27) for each internal grid point as follow:

$$\frac{\partial u_{63}^{*,\text{num}}}{\partial x} = \frac{1}{h}[\sum_{p=1}^{125} k_p[a_p u_p^{*,\text{num}} + (1-a_p)u_p^{**,\text{num}}] - \bar{f}], \tag{32}$$

if the central stencil point belongs to material $*$ ($a_{63} = 1$) and

$$\frac{\partial u_{63}^{**,\text{num}}}{\partial x} = \frac{1}{h}[\sum_{p=1}^{125} k_p[a_p u_p^{*,\text{num}} + (1-a_p)u_p^{**,\text{num}}] - \bar{f}], \tag{33}$$

if the central stencil point belongs to material $**$ ($a_{63} = 0$).

The calculation of the derivatives $\frac{\partial u^{\text{num}}}{\partial y}$ and $\frac{\partial u^{\text{num}}}{\partial z}$ can be done similar to the calculation of the derivative $\frac{\partial u^{\text{num}}}{\partial x}$ as described above.

Remark 6. If any of the grid points included into the stencil is located on the boundary with the Dirichlet boundary conditions then for this point p in Eqs. (32) and (33) we use the exact value of $u_p^{*,\text{num}}$ or $u_p^{**,\text{num}}$ defined by the boundary conditions. In the case of the Neumann boundary conditions, the procedure can be modified similar to that in our paper [28] for OLTEM with irregular boundaries and the Neumann boundary conditions.

It is interesting to note that for homogeneous materials the post-processing procedure described above can be also used for the calculation of the spatial derivatives without the application of the partial differential equation as in other post-processing techniques (e.g., see [37–39] for finite and isogeometric elements). Let us assume that we can calculate the derivative $\frac{\partial u^{\text{num}}}{\partial x}$ at the internal grid point in terms of the values of the function u^{num} at the neighboring grid points. For simplicity, we will use a uniform Cartesian mesh and 125 grid points for the calculation of the derivative $\frac{\partial u_{63}^{\text{num}}}{\partial x}$ at the central grid point (see Fig. 1a) as follows:

$$-h\frac{\partial u_{63}^{\text{num}}}{\partial x} + \sum_{p=1}^{125} k_p u_p^{\text{num}} = 0 \tag{34}$$

with the following local truncation error:

$$e_p = -h\frac{\partial u_{63}}{\partial x} + \sum_{p=1}^{125} k_p u_p \,. \tag{35}$$

Repeating the procedure described in Section 3.1 without the use of Eqs. (14) and (15) and zeroing the corresponding coefficients b_p in the Taylor expansion of the local truncation error e_p, we can show that the maximum possible order of the local truncation error, Eq. (35), without the application of the Poisson equation is 5. For example, for square meshes we can zero all coefficients b_p up to the fifth order with respect to h except one b_p coefficient

corresponding to the fifth order. This non-zero coefficient yields the following local truncation error, Eq. (35), without the use of PDE:

$$e_p = \frac{h^5}{30}\frac{\partial^5 u_{63}}{\partial x^5} + O(h^6)\,. \tag{36}$$

In this case the order of the local truncation error corresponds to that for the well-known finite-difference approximation of the first order derivative $\frac{\partial u^{\rm num}}{\partial x}$ with 5 grid points along x-axis. Comparing Eqs. (31) and (36) we can see that the use of PDE for post-processing improves the accuracy of the spatial derivative by 6 (!) orders for the same 125-point compact stencils. We should also mention that the approximation given by Eq. (34) cannot be used for the stencils with interfaces (as those in Fig. 1b).

To summarize, the proposed post-processing procedure provides the optimal accuracy of the spatial derivatives of primary functions calculated with the help of compact stencils. It can be developed with or without the use of PDEs. However, the use of PDEs significantly improves the accuracy of the spatial derivatives for the given stencils. Finally, the post-processing procedure developed can be independently used with any known numerical technique (e.g., with finite elements).

Remark 7. Despite the fact that we have applied the proposed post-processing technique to the stencils defined on Cartesian meshes, it can be also used for non-uniform locations of grid points with the corresponding coefficients $r_{x,p}$, $r_{y,p}$, $r_{z,p}$ in Eq. (6) (similar to OLTEM developed in our papers [23,25,28] for irregular boundaries).

5. Numerical examples

In this section the computational efficiency of OLTEM with unfitted meshes and the 125-point stencils developed for the solution of the 3-D Poisson equation with discontinuous coefficients will be demonstrated and compared with conventional linear and high order (up to 7th order) tetrahedral finite elements. For finite element calculations, the commercial finite element software COMSOL [40] with isoparametric finite elements and geometrically conforming meshes is used. In order to compare the accuracy of OLTEM with FEM, the following errors are considered below. The relative error e_w^j for the function w at the jth grid point is defined as:

$$e_w^j = \frac{\mid w_j^{\rm num} - w_j^{\rm exact} \mid}{w_{max}^{\rm exact}}\,, \qquad j = 1, 2, \ldots, N. \tag{37}$$

The maximum relative error e_w^{max} for the function w is defined as:

$$e_w^{max} = \max_j e_w^j\,, \qquad j = 1, 2, \ldots, N. \tag{38}$$

In Eqs. (37)–(38) the superscripts 'num' and 'exact' correspond to the numerical and exact solutions, N is the total number of the grid points used in calculations, $w_{max}^{\rm exact}$ is the maximum absolute value of the exact solution over the entire domain for the function w. We also use the L^2 error norm for finite elements (e.g., see [41]) and the l^2 error norm (e.g., see [42]) for OLTEM:

$$e_w^{l^2} = \{dx\,dy\,dz \sum_{i=0}^{N_x}\sum_{j=0}^{N_y}\sum_{k=0}^{N_k}[w^{\rm num}(x_i, y_j, z_k) - w^{\rm exact}(x_i, y_j, z_k)]^2\}^{\frac{1}{2}} / |w^{\rm exact}|_{L^2}\,, \tag{39}$$

where N_x, N_y and N_k are the numbers of Cartesian grid points along x, y and z-axes, x_i, y_j and z_k are the coordinates of Cartesian grid points, respectively. As function w in Eqs. (37)–(39) we consider u, $\frac{\partial u}{\partial x}$, $\frac{\partial u}{\partial y}$ and $\frac{\partial u}{\partial z}$.

5.1. 3-D bi-material cube with a spherical inclusion

The focus of the paper is OLTEM for interface problems. Therefore, here we solve the problem with a regular boundary and a curved interface. The development of OLTEM for domains with curved boundaries is considered in our papers [25,28]. Consider the 3-D Poisson equation with discontinuous coefficients for the bi-material cube with dimensions $2 \times 2 \times 2$ as shown in Fig. 2a. The cube consists of a spherical inclusion (subdomain Ω_I) at the center of the cube and the matrix (subdomain Ω_{II}) with the circular interface described by the following equation:

$$x^2 + y^2 + z^2 = r^2\,, \tag{40}$$

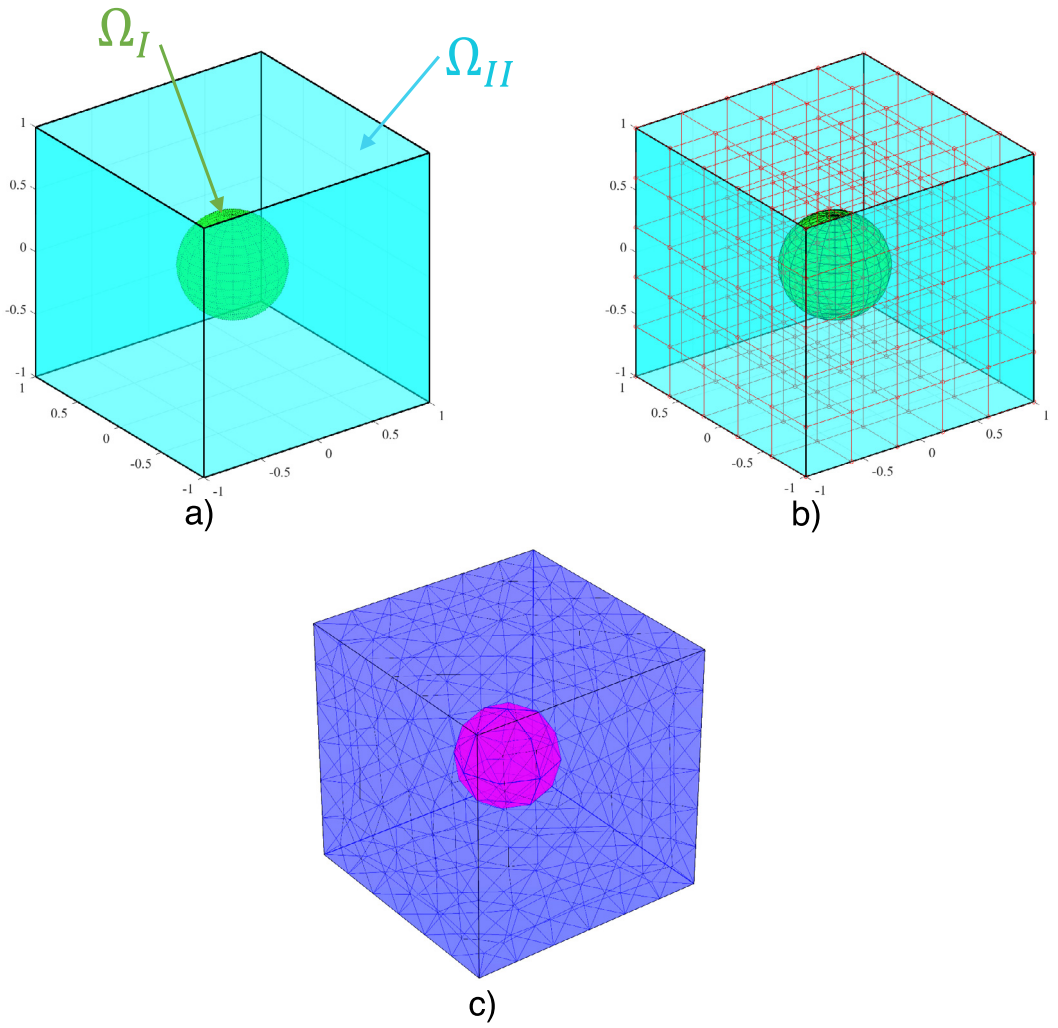

Fig. 2. A 3-D cube with a spherical inclusion (a), examples of an unfitted Cartesian mesh for OLTEM (b) and a conforming tetrahedral finite element mesh generated by the commercial software COMSOL (c).

where $r = 0.4$ is the radius of the circular interface. The following material properties are assumed: $c_I = \frac{1}{50}; \frac{1}{100}; \frac{1}{200}; 50; 100; 200$ in Ω_I and $c_{II} = 1$ in Ω_{II} with the material contrasts $\frac{c_I}{c_{II}} = \frac{1}{50}; \frac{1}{100}; \frac{1}{200}; 50; 100; 200$. Using the method of manufactured solution, the following exact solution to the Poisson equation is selected:

$$u(x,y,z) = \begin{cases} \cos(\frac{x^2}{r^2} + \frac{y^2}{r^2} + \frac{z^2}{r^2}) & \text{in} \quad \Omega_I \\ \\ \frac{c_I}{c_{II}} \cos(\frac{x^2}{r^2} + \frac{y^2}{r^2} + \frac{z^2}{r^2}) - (\frac{c_I}{c_{II}} - 1)\cos(1) & \text{in} \quad \Omega_{II} \end{cases} \tag{41}$$

This solution meets the interface conditions, Eq. (2), with zero jumps $\delta_1 = \delta_2 = 0$. The source terms can be calculated by the substitution of the exact solution into the Poisson equation, Eq. (1), and are given below: $f_I(x,y,z) = -2c_I[\frac{2}{r^2}(\frac{x^2}{r^2} + \frac{y^2}{r^2} + \frac{z^2}{r^2})\cos(\frac{x^2}{r^2} + \frac{y^2}{r^2} + \frac{z^2}{r^2}) + (\frac{3}{r^2})\sin(\frac{x^2}{r^2} + \frac{y^2}{r^2} + \frac{z^2}{r^2})] \quad \text{in} \quad \Omega_I$; $f_{II}(x,y,z) = -2c_I[\frac{2}{r^2}(\frac{x^2}{r^2} + \frac{y^2}{r^2} + \frac{z^2}{r^2})\cos(\frac{x^2}{r^2} + \frac{y^2}{r^2} + \frac{z^2}{r^2}) + (\frac{3}{r^2})\sin(\frac{x^2}{r^2} + \frac{y^2}{r^2} + \frac{z^2}{r^2})] \quad \text{in} \quad \Omega_{II}$. The Dirichlet boundary conditions along all faces of the cube are imposed according to the exact solution, Eq. (41). The problem is solved by OLTEM with the 125-point stencils as well as by linear and high order (up to the 7th order) finite elements for different material contrasts $\frac{c_I}{c_{II}}$. To get a high accuracy for OLTEM with cut 125-point stencils located close to the boundary,

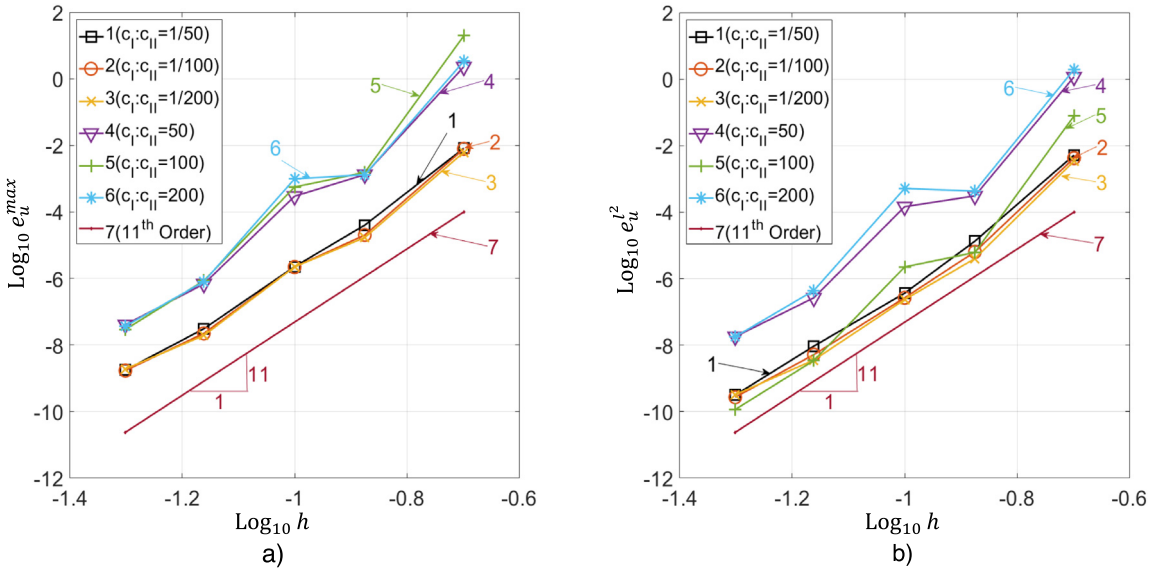

Fig. 3. The maximum relative error e_u^{max} (a) and the l^2 error norm $e_u^{l^2}$ (b) as a function of the mesh size h at mesh refinement in the logarithmic scale. The numerical solutions of the 3-D Poisson equation for the cube with the spherical inclusion (see Fig. 2a) are obtained by OLTEM on square ($b_y = 1$ and $b_z = 1$) Cartesian meshes with the following material contrasts: $\frac{c_I}{c_{II}} = \frac{1}{50}$ (curve 1), $\frac{c_I}{c_{II}} = \frac{1}{100}$ (curve 2), $\frac{c_I}{c_{II}} = \frac{1}{200}$ (curve 3), $\frac{c_I}{c_{II}} = 50$ (curve 4), $\frac{c_I}{c_{II}} = 100$ (curve 5) and $\frac{c_I}{c_{II}} = 200$ (curve 6). The reference line 7 designates the 11th order of convergence.

the high-order numerical boundary conditions similar to those developed in our papers [24,35] are used. Fig. 2b,c shows a typical unfitted Cartesian mesh with aspects ratios $b_y = b_z = 1$ used for OLTEM as well as a typical conforming tetrahedral finite element mesh.

First, we present the application of OLTEM to the solution of the Poisson equation for heterogeneous materials with different material contrasts $\frac{c_I}{c_{II}}$. Fig. 3 shows the maximum relative error e_u^{max} and the l^2 error norm $e_u^{l^2}$ as a function of the mesh size h in the logarithmic scale for OLTEM with the 125-point stencils and the material contrasts $\frac{c_I}{c_{II}} = \frac{1}{50}; \frac{1}{100}; \frac{1}{200}; 50; 100; 200$. As can be seen from Fig. 3, OLTEM yields convergent results with the order of convergence close to eleven for all material contrasts. The reference line (line 7) corresponds to the 11th order of convergence. These observations are in agreement with the theoretical results in the previous Section 3.

Next, we present the accuracy comparison of OLTEM with linear and high order (up to the 7th order — the highest order in COMSOL) finite elements for the material contrast $\frac{c_I}{c_{II}} = \frac{1}{50}$ (similar results can be also obtained for other material contrasts). Fig. 4 shows the maximum relative errors e_u^{max} and the errors $e_u^{L^2}$ in the L^2 norm as a function of the number N of degrees of freedom in the logarithmic scale for the numerical results obtained by OLTEM and by finite elements. As can be seen from Fig. 4, at the same N the numerical results obtained by OLTEM are much more accurate than those obtained by linear and higher order finite elements (see Fig. 4a,b). This increase in accuracy by OLTEM is impressive considering the fact that higher order finite elements have much wider stencils (e.g., $15 \times 15 \times 15 = 3375$-point stencils for the 7th order finite elements) compared to those for OLTEM (the width of the stencils for OLTEM corresponds to that for quadratic finite elements) and require a much greater computation time. We should also mention that at an accuracy of 0.1%, OLTEM with the 125-point stencils reduces the number N of degrees of freedom by a factor of greater than 180 for the maximum relative error e_u^{max} and greater than 27 for the L^2 error norm $e_u^{L^2}$ compared to that for quadratic finite elements. This will lead to an extremely large reduction in the computation time for OLTEM compared to quadratic finite elements at a given accuracy.

A study of the stability of the numerical results with respect to grid positioning is shown for OLTEM in Fig. 5. For this study, we solve the test problem with the material contrast $\frac{c_I}{c_{II}} = \frac{1}{50}$ on 501 Cartesian meshes with the mesh sizes $h_i = \bar{h}_1 + \frac{(\bar{h}_2 - \bar{h}_1)(i-1)}{500}$ and a very small variation of the mesh size h where $\bar{h}_1 = 2/15$, $\bar{h}_2 = 2/20$

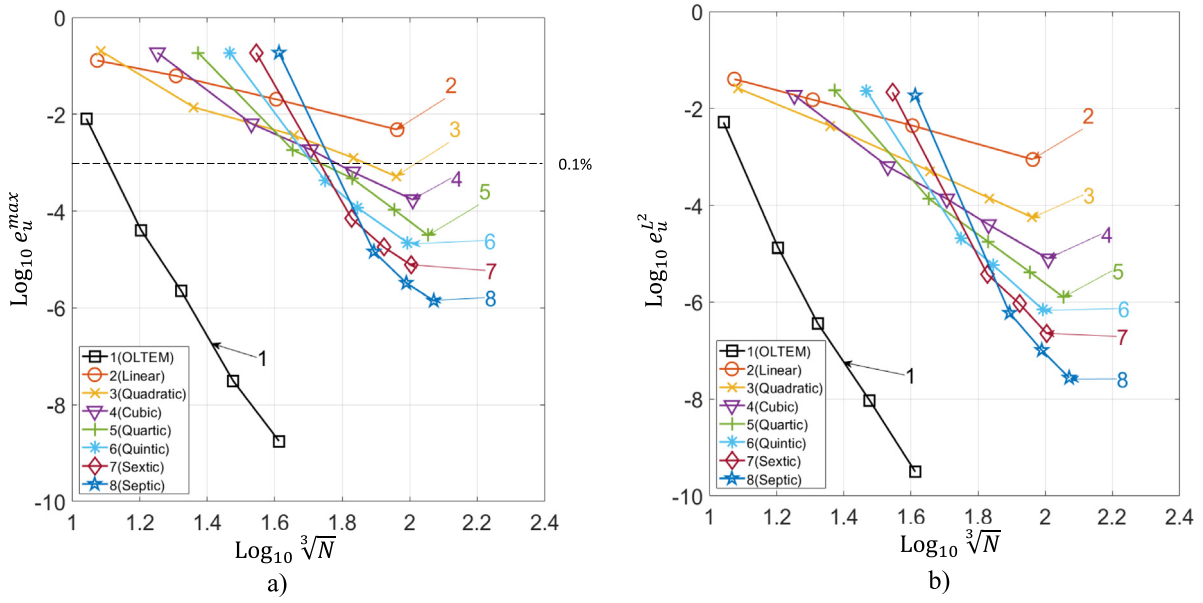

Fig. 4. The maximum relative error e_u^{max} (a) and the L^2 error norm $e_u^{L^2}$ (b) as a function of $\sqrt[3]{N}$ at mesh refinement in the logarithmic scale (N is the number of degrees of freedom). The numerical solutions of the 3-D Poisson equation for the cube with the spherical inclusion and the material contrast $\frac{c_I}{c_{II}} = \frac{1}{50}$ (see Fig. 2a) are obtained by OLTEM on unfitted square ($b_y = 1$ and $b_z = 1$) Cartesian meshes (curve 1) as well as by linear and high-order tetrahedral finite elements (curves 2–8) on conforming meshes. Curves 2, 3, …,8 correspond to linear, quadratic, …, and the 7th order finite elements.

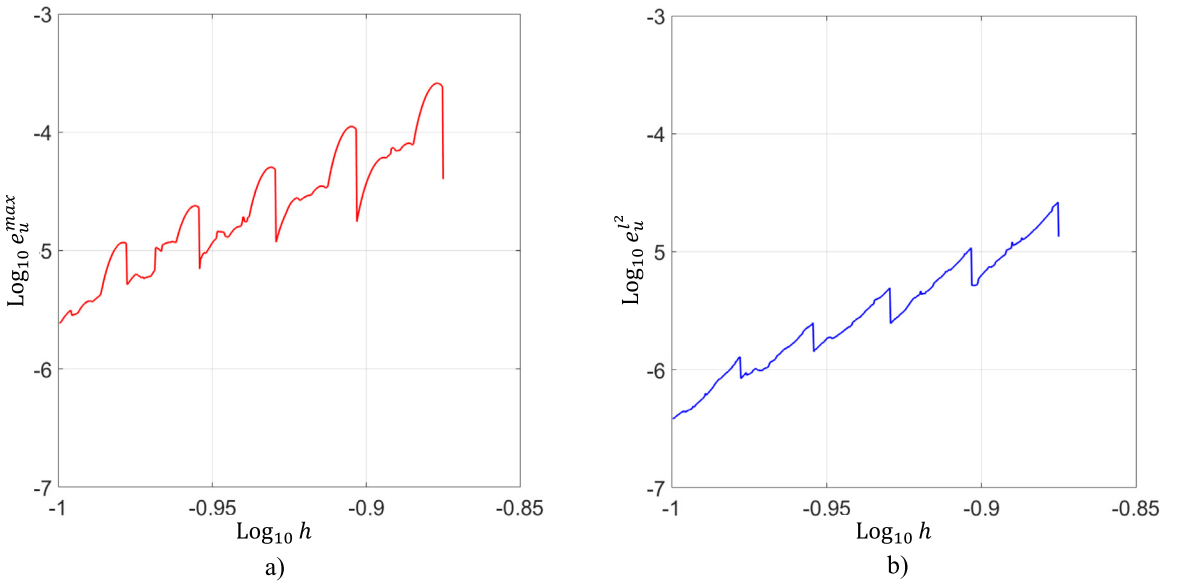

Fig. 5. The logarithm of the maximum relative errors e_u^{max} (a) and the l^2 error norm $e_u^{l^2}$ (b) as a function of the mesh size h. The numerical solutions of the 3-D Poisson equation for the cube with the spherical inclusion (see Fig. 2a) are obtained by OLTEM on unfitted square ($b_y = 1$ and $b_z = 1$) Cartesian meshes with the material contrast $\frac{c_I}{c_{II}} = \frac{1}{50}$. Each curve is calculated on 501 meshes; see the text.

and $i = 1, 2, \ldots, 501$. For these meshes, three grid planes always coincide with the left, bottom and rear faces of the cubical domain and at the small variation of the mesh size h we have very different locations of the circular

interface with respect to the grid points. The curves in Fig. 5 correspond to curves 1 in Fig. 3. As can be seen from Fig. 5, the numerical results obtained by OLTEM on these meshes converge with the decrease in the grid size h. Small oscillations in Fig. 5 decrease with the decrease in the mesh size. This oscillatory behavior can be explained by the fact that at small variations of the mesh size h, there is a discontinuous change in the location of the grid points with respect to the interface (e.g., some grid points that belong to one material for the previous mesh can belong to another material for the next mesh; this change in location leads to the discontinuous change of some stencils equations for the meshes with a small difference in h). Note that small oscillations in numerical convergence curves are typical for many numerical techniques at small variations of h. For example, the change in the angles of finite elements at small variations of the element size h also leads to such oscillations in convergence curves for finite element techniques.

The application of the new post-processing procedure for the calculation of the spatial derivatives of numerical solutions is presented in Figs. 6 and 7. Here, we solve the test problem with the material contrast $\frac{c_I}{c_{II}} = \frac{1}{50}$ by OLTEM with the 125-point stencils as well as by linear and high order finite elements and compare the accuracy of the spatial derivatives $\frac{\partial u^{\text{num}}}{\partial x}$, $\frac{\partial u^{\text{num}}}{\partial y}$ and $\frac{\partial u^{\text{num}}}{\partial z}$ of the numerical solutions u^{num}. Figs. 6 and 7 show the maximum relative errors $e^{max}_{\frac{\partial u}{\partial x}}$, $e^{max}_{\frac{\partial u}{\partial y}}$, $e^{max}_{\frac{\partial u}{\partial z}}$ and the errors $e^{L^2}_{\frac{\partial u}{\partial x}}$, $e^{L^2}_{\frac{\partial u}{\partial y}}$, $e^{L^2}_{\frac{\partial u}{\partial z}}$ in the L^2 norm as a function of the number N of degrees of freedom for different techniques. As can be seen from Figs. 6 and 7, at the same N the spatial derivatives $\frac{\partial u^{\text{num}}}{\partial x}$, $\frac{\partial u^{\text{num}}}{\partial y}$ and $\frac{\partial u^{\text{num}}}{\partial z}$ obtained by OLTEM are much more accurate than those obtained by linear and high-order (up to the 7th order) finite elements for the both selected error norms. To compare OLTEM with the 125-point stencils and quadratic finite elements (these techniques have similar computational costs), let us estimate the number of degrees of freedom required for an accuracy of 0.1% with these methods. In order to do this estimation, we need to find the intersection of curves 1 and 3 in Figs. 6 and 7 with the horizontal line -3 along the vertical axis corresponding to the accuracy of 0.1% (we extrapolated the curves 3 using the constant slope related to the last two finest meshes). The numerical results in Figs. 6 and 7 show that at an accuracy of 0.1% for the spatial derivatives, OLTEM reduces the number N of degrees of freedom by a factor of greater than 3.8×10^6 for the maximum relative error and greater than 900 for the L^2 error norm compared to that for quadratic finite elements. This reduction in the number of degrees of freedom will lead to an extremely large reduction in the computation time for the calculation of the spatial derivatives by OLTEM compared to those obtained by finite elements at a given accuracy.

5.2. 3-D cube with three spherical inclusions

Let us consider a cube of dimensions $2 \times 2 \times 2$ with three spherical inclusions (subdomains Ω_i, $i = 1, 2, 3$) and the matrix (subdomain Ω_4); see Fig. 8. The three circular interfaces are described by the following equation:

$$x^2 + y^2 + z^2 = r_i^2, \qquad i = 1, 2, 3 \tag{42}$$

where $r_1 = 0.4$, $r_2 = 0.3$, $r_3 = 0.2$ are the radii of the three circular interfaces. The centers of the inclusions are located at the points with the following coordinates: $(-0.2, 0.2, -0.4)$, $(0.6, -0.6, 0.2)$, $(-0.6, 0.6, 0.4)$. The following material properties of the inclusions and the matrix are assumed: $c_1 = 2$, $c_2 = 5$, $c_3 = 10$, $c_4 = 1$. Using the method of manufactured solution, the following exact solution to the Poisson equation is selected in the cubic domain:

$$u(x, y, z) = \begin{cases} \cos(\alpha_1 x)\cos(\beta_1 y)\cos(\gamma_1 z) & \text{in} \quad \Omega_1, \Omega_2 \text{ and } \Omega_3 \\ \\ \cos(\alpha_2 x)\cos(\beta_2 y)\cos(\gamma_2 z) & \text{in} \quad \Omega_4 \end{cases}, \tag{43}$$

with $\alpha_1 = 4$, $\beta_1 = 7$, $\gamma_1 = 15$ for the inclusions and $\alpha_2 = 5$, $\beta_2 = 20$, $\gamma_2 = 17$ for the matrix. Inserting this exact solution, Eq. (43), in the interface conditions, Eq. (2) and the Poisson equation, Eq. (1), we can find the jumps δ_1 and δ_2 at the interfaces as well as the source terms $f_l(\boldsymbol{x})$ ($l = 1, 2, 3, 4$). The Dirichlet boundary conditions along all faces of the cube are imposed according to the exact solution, Eq. (43). The problem is solved by OLTEM with the 125-point stencils. To get a high accuracy for OLTEM with cut 125-point stencils located close to the boundary, the high-order numerical boundary conditions similar to those developed in our papers [24,35] are used. Fig. 9 shows the maximum relative error e_u^{max} and the l^2 error norm $e_u^{l^2}$ as a function of the mesh size h in the logarithmic scale for OLTEM with the 125-point stencils. As can be seen from Fig. 9, OLTEM yields convergent results with

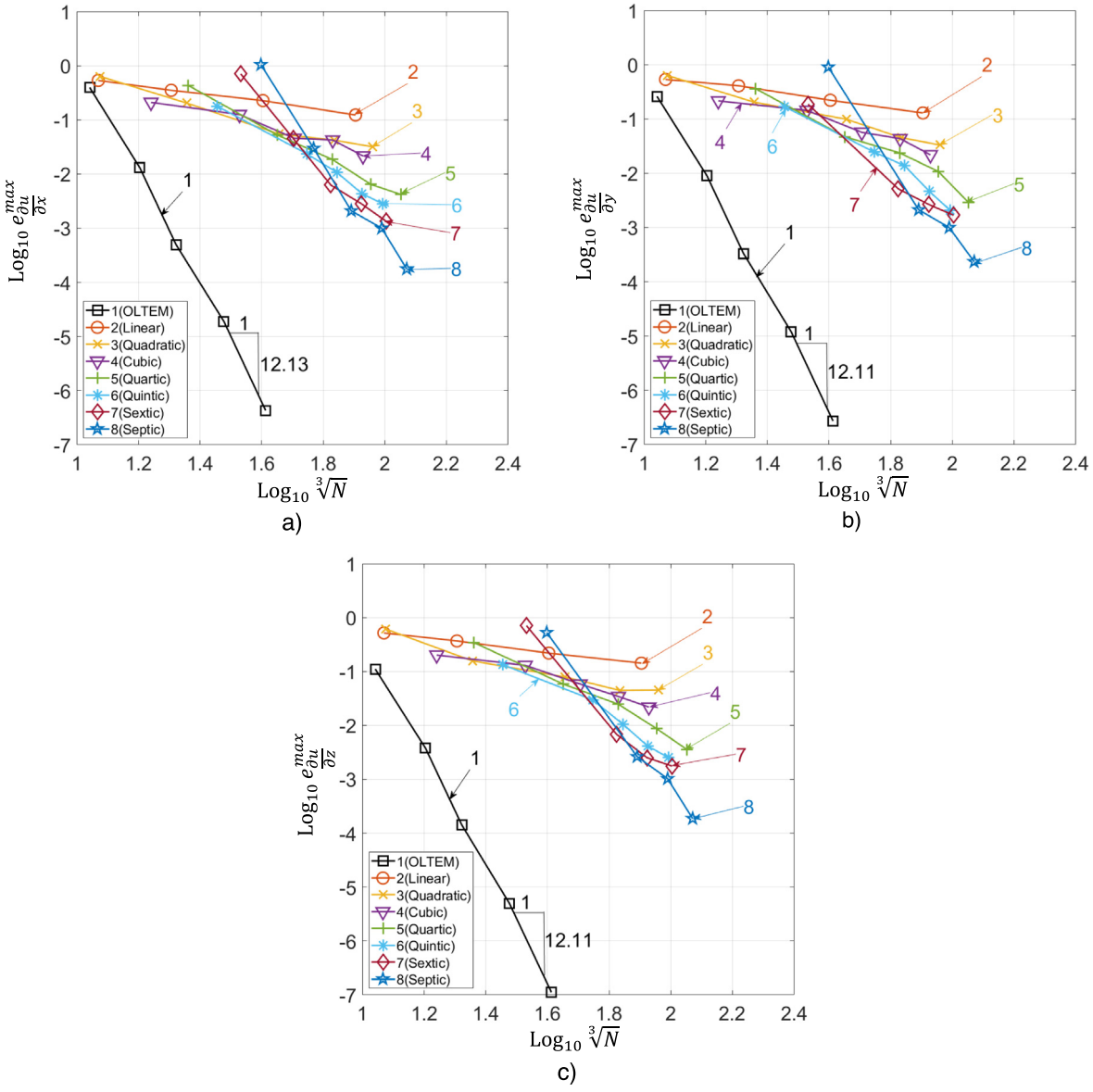

Fig. 6. The maximum relative errors for the spatial derivatives $e^{max}_{\frac{\partial u}{\partial x}}$ (a), $e^{max}_{\frac{\partial u}{\partial y}}$ (b), $e^{max}_{\frac{\partial u}{\partial z}}$ (c) as a function of $\sqrt[3]{N}$ at mesh refinement in the logarithmic scale (N is the number of degrees of freedom). The numerical solutions of the 3-D Poisson equation for the cube with the spherical inclusion and the material contrast $\frac{c_I}{c_{II}} = \frac{1}{50}$ (see Fig. 2a) are obtained by OLTEM on unfitted square ($b_y = 1$ and $b_z = 1$) Cartesian meshes (curve 1) as well as by linear and high-order tetrahedral finite elements (curves 2–8) on conforming meshes. Curves 2, 3, ...,8 correspond to linear, quadratic, ..., and the 7th order finite elements.

the order of convergence close to eleven. The reference line (line 2) corresponds to the 11th order of convergence. These observations are in agreement with the theoretical results in the previous Section 3.

6. Concluding remarks

OLTEM with the 125-point stencils for heterogeneous materials with smooth irregular interfaces and unfitted Cartesian meshes has been developed for the Poisson equation in the general 3-D case. The main idea in the development of OLTEM is to provide the maximum possible accuracy of discrete equations after the space

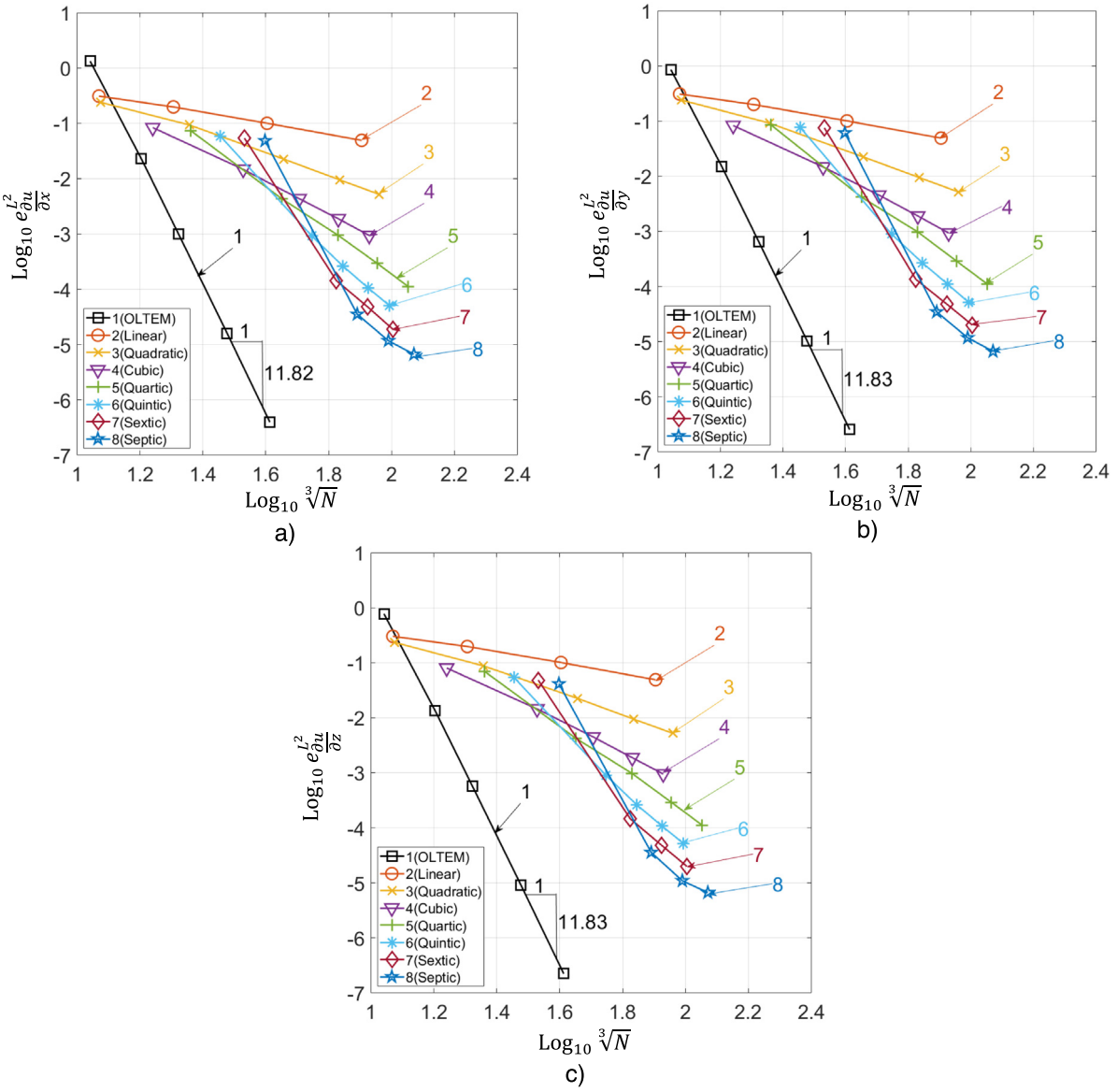

Fig. 7. The L^2 error norm of the spatial derivatives $e^{L^2}_{\frac{\partial u}{\partial x}}$ (a), $e^{L^2}_{\frac{\partial u}{\partial y}}$ (b), $e^{L^2}_{\frac{\partial u}{\partial z}}$ (c) as a function of $\sqrt[3]{N}$ at mesh refinement in the logarithmic scale (N is the number of degrees of freedom). The numerical solutions of the 3-D Poisson equation for the cube with the spherical inclusion and the material contrast $\frac{c_I}{c_{II}} = \frac{1}{50}$ (see Fig. 2a) are obtained by OLTEM on unfitted square ($b_y = 1$ and $b_z = 1$) Cartesian meshes (curve 1) as well as by linear and high-order tetrahedral finite elements (curves 2–8) on conforming meshes. Curves 2, 3, …,8 correspond to linear, quadratic, …, and the 7th order finite elements.

discretization of PDEs. The derivation of OLTEM is based on the minimization of the local truncation error of the stencil (discrete) equations using the entire PDEs. The global system of equations for OLTEM has the non-symmetric stiffness matrix and can be solved with an iterative solver (e.g., we use the built-in Matlab solver ‘gmres’ [36] without preconditioners). At similar numbers of degrees of freedom and similar widths of the stiffness matrices, the accuracy of OLTEM is much higher than that for existing numerical techniques. In contrast to our previous publications, for the first time we have developed OLTEM with 125-point stencils for irregular geometry in the general 3-D case.

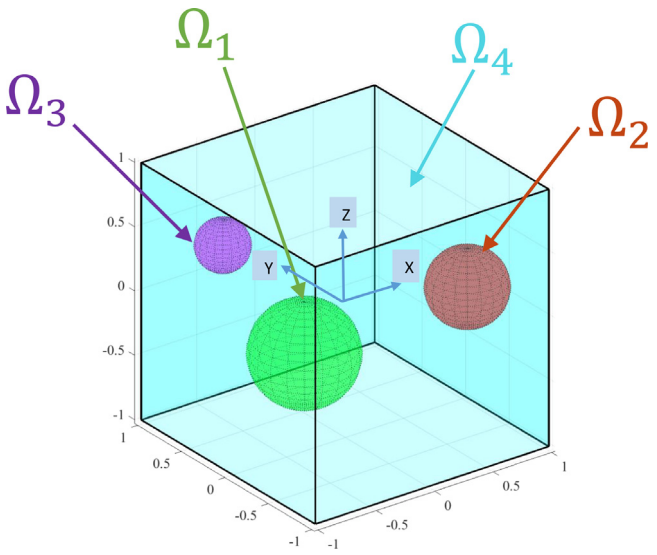

Fig. 8. A 3-D cube with three spherical inclusions.

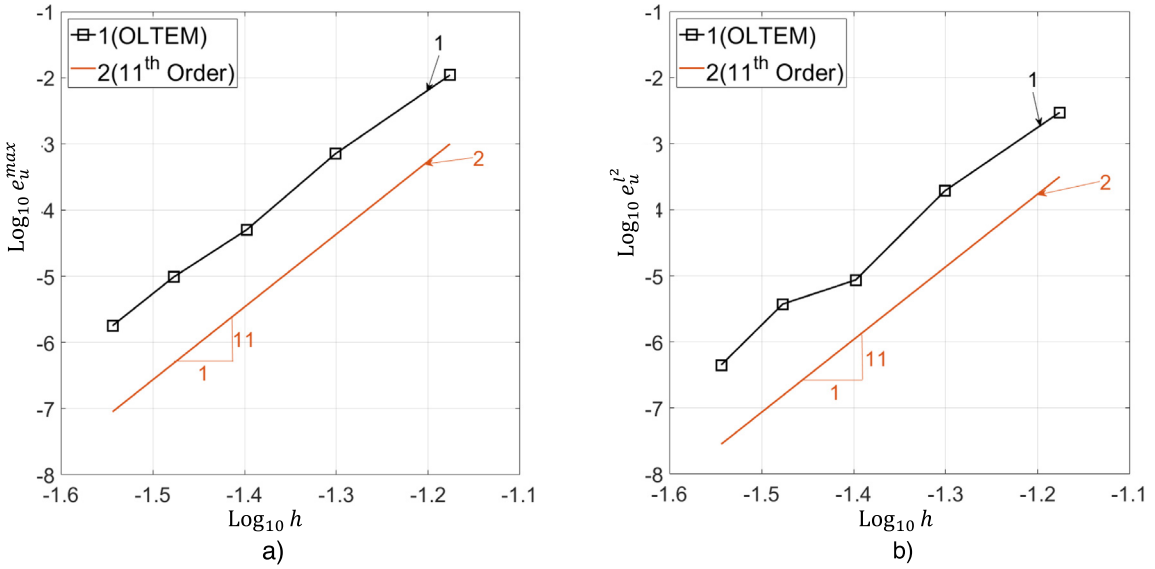

Fig. 9. The maximum relative error e_u^{max} (curve 1 in a) and the l^2 error norm $e_u^{l^2}$ (curve 1 in b) as a function of the mesh size h at mesh refinement in the logarithmic scale. The numerical solutions of the 3-D Poisson equation for the cube with the three spherical inclusions (see Fig. 8) are obtained by OLTEM on unfitted square ($b_y = 1$ and $b_z = 1$) Cartesian meshes. The reference line 2 designates the 11th order of convergence.

The main advantages of the developed numerical technique can be summarized as follows:

- OLTEM with the 125-point stencils (similar to those for quadratic finite elements) provides an extremely large increase in accuracy for the Poisson equation for heterogeneous materials with irregular interfaces. Compared with the existing finite element techniques with quadratic elements that provide the third order of accuracy on conforming and unfitted meshes (e.g., see [3,5,7–12,14–16]), OLTEM provides the 11th order of accuracy with an extremely large increase by 8 orders at similar stencils.

- OLTEM uses trivial unfitted Cartesian meshes independent of the location of interfaces. These unfitted meshes significantly simplify the preparation of input data for numerical simulations of heterogeneous materials.
- OLTEM does not approximate irregular geometry of interfaces. The exact interface conditions, Eq. (2), are used at a small number of interface points located on the exact interface. For regular geometry without interfaces, OLTEM usually provides a higher order of convergence compared to that for curved interfaces, e.g., see our papers [30,31].
- In contrast to the different modifications of finite element techniques with unfitted meshes, OLTEM does not introduce additional unknowns for the description of the interface conditions. OLTEM uses just the regular unknowns at the internal Cartesian grid points. The sparse structure of the global discrete equations for OLTEM is the same for homogeneous (without interfaces) and heterogeneous (with interfaces) materials, i.e., the difference is only in the values of the coefficients of the global matrices for homogeneous and heterogeneous materials.
- OLTEM with the 125-point stencils and unfitted meshes provides much more accurate results than high-order (up to the 7th order — the maximum order implemented in the commercial finite element software COMSOL) finite elements with much wider stencils (e.g., 3375-point stencils for the 7th order finite elements). At an accuracy of 0.1%, OLTEM reduces the number of degrees of freedom by $27-180$ times compared to quadratic finite elements for the considered test problem with the spherical interface.
- In contrast to the finite difference method (see also a short discussion in the Introduction), OLTEM does not need the approximation of the normal derivatives for the grid points located close to the interfaces, the width of the homogeneous and heterogeneous stencils is the same, as well as OLTEM provides much a higher order of accuracy for interface problems compared to that for known finite difference techniques, e.g., see [17–22] and others.
- A new post-processing procedure with 125-point stencils (similar to those used in basic computations) has been developed for the calculation of the spatial derivatives of the primary function. It is based on the solution of a small local system of algebraic equations and the use of the original PDE (the Poisson equation). It was shown that the use of PDE for the 125-point stencils improves the accuracy of the spatial derivatives by 6 orders compared to the calculations without the use of PDE as in the existing numerical techniques. Due to the new post-processing procedure, the difference in accuracy for the spatial derivatives calculated by OLTEM with the 125-point stencils and by high-order (up to the 7th order) finite elements is much greater than that for the primary function. At an accuracy of 0.1% for the spatial derivatives, OLTEM reduces the number of degrees of freedom by $900-4\cdot10^6$ times compared to quadratic finite elements for the considered test problem with the spherical interface. The developed post-processing procedure can be easily extended to unstructured meshes and can be independently used with existing numerical techniques (e.g., with finite elements).

In the future, we plan to develop OLTEM with adaptive mesh refinement similar to $h-$ and $p-$ mesh refinements for finite elements (it was shown in papers [27,30] that OLTEM can easily combine different stencils). We plan to use quadtrees/octrees meshes that allow a simple refinement strategy with Cartesian meshes. Currently, we analyze smooth interfaces without singular points that intersects the 125-point cell as well as we assume sufficiently smooth exact solutions. The extension of OLTEM to non-smooth solutions as well as to non-smooth interfaces that also includes the case of singular points with three or more different materials in contact will be considered. We should mention that the numerical results for the 1-D wave equation in our paper [34] show that OLTEM can accurately solve the problems with propagating discontinuity. However, we expect a lower order of convergence of OLTEM for the problems with non-smooth solutions compared to that for smooth solutions. The extension of OLTEM to other PDEs with discontinuous coefficients as well as to non-linear PDEs will be also considered in the future. We plan to extend the new post-processing procedure with OLTEM to other PDEs.

Declaration of competing interest

The authors declare that they have no known competing financial interests or personal relationships that could have appeared to influence the work reported in this paper.

Data availability

Data will be made available on request.

Acknowledgments

The research has been supported in part by Sandia, United States (contract 2416989), by the National Science Foundation grant CMMI-1935452, and by Texas Tech University, United States. Sandia National Laboratories is a multi-mission laboratory managed and operated by National Technology & Engineering Solutions of Sandia, LLC (NTESS), a wholly owned subsidiary of Honeywell International Inc., for the U.S. Department of Energy's National Nuclear Security Administration (DOE/NNSA) under contract DE-NA0003525. This written work is authored by an employee of NTESS. The employee, not NTESS, owns the right, title and interest in and to the written work and is responsible for its contents. Any subjective views or opinions that might be expressed in the written work do not necessarily represent the views of the U.S. Government. The publisher acknowledges that the U.S. Government retains a non-exclusive, paid-up, irrevocable, world-wide license to publish or reproduce the published form of this written work or allow others to do so, for U.S. Government purposes. The DOE will provide public access to results of federally sponsored research in accordance with the DOE Public Access Plan.

Appendix A. The coefficients b_p used in Eq. (16) for the 125-point stencils.

The first 10 coefficients b_p ($p = 1, 2, \ldots, 10$) are presented below. Please see also Appendix B and the attached file b-coef.nb.

$$b_1 = \sum_{j=1}^{125} a_j k_j + \sum_{j=1}^{81} q_{1,j}$$

$$b_2 = \sum_{j=1}^{125} (1 - a_j) k_j - \sum_{j=1}^{81} q_{1,j}$$

$$b_3 = \sum_{j=1}^{125} b_z a_j (r_{z,j} - dz_G) k_j + \sum_{j=1}^{81} (d_{z,j} q_{1,j} + c_* n_{z,j} q_{2,j})$$

$$b_4 = \sum_{j=1}^{125} b_z (1 - a_j)(r_{z,j} - dz_G) k_j - \sum_{j=1}^{81} (d_{z,j} q_{1,j} + c_{**} n_{z,j} q_{2,j})$$

$$b_5 = \sum_{j=1}^{125} b_y a_j (r_{y,j} - dy_G) k_j + \sum_{j=1}^{81} (d_{y,j} q_{1,j} + c_* n_{y,j} q_{2,j})$$

$$b_6 = \sum_{j=1}^{125} b_y (1 - a_j)(r_{y,j} - dy_G) k_j - \sum_{j=1}^{81} (d_{y,j} q_{1,j} + c_{**} n_{y,j} q_{2,j})$$

$$b_7 = \sum_{j=1}^{125} b_x a_j (r_{x,j} - dx_G) k_j + \sum_{j=1}^{81} (d_{x,j} q_{1,j} + c_* n_{x,j} q_{2,j})$$

$$b_8 = \sum_{j=1}^{125} b_x (1 - a_j)(r_{x,j} - dx_G) k_j - \sum_{j=1}^{81} (d_{x,j} q_{1,j} + c_{**} n_{x,j} q_{2,j})$$

$$b_9 = \sum_{j=1}^{125} \frac{1}{2} a_j [b_z^2 (r_{z,j} - dz_G)^2 - (r_{x,j} - dy_G)^2] k_j + \sum_{j=1}^{81} [\frac{1}{2}(d_{z,j}^2 - d_{x,j}^2) q_{1,j} + c_* (d_{z,j} n_{x,j} - d_{z,j} n_{x,j}) q_{2,j}]$$

$$b_{10} = \sum_{j=1}^{125} \frac{1}{2} (1 - a_j)[b_z^2 (r_{z,j} - dz_G)^2 - (r_{x,j} - dy_G)^2] k_j - \sum_{j=1}^{81} [\frac{1}{2}(d_{z,j}^2 - d_{x,j}^2) q_{1,j} + c_{**} (d_{z,j} n_{x,j} - d_{z,j} n_{x,j}) q_{2,j}]$$

Appendix B. The explicit form of Eqs. (23) for the determination of the stencil coefficients.

The coefficients b_i in Eq. (16) can be represented as a linear function of the stencil coefficients k_j, $q_{1,j}$ and $q_{1,j}$ as follows:

$$b_i = \sum_{j=1}^{125} s_{ij} k_j + \sum_{j=1}^{81} (c_{ij}^1 q_{1,j} + c_{ij}^2 q_{2,j}), \qquad i = 1, 2, \ldots, 578, \tag{B.1}$$

where the coefficients s_{ij}, c^1_{ij} and c^2_{ij} can be found from the expressions for the coefficients b_i; see Appendix A and the attached file b-coef.nb.

Then using Eq. (B.1), the local system of linear algebraic equations for finding the stencil coefficients, Eqs. (23), can be rewritten as follows:

$$\begin{aligned}
\frac{\partial \bar{R}}{\partial k_m} &= \sum_{l=1}^{200} \lambda_l \frac{\partial b_l}{\partial k_m} + 2\left[\sum_{p=201}^{242} b_p \frac{\partial b_p}{\partial k_m} + h_1 \sum_{p=243}^{288} b_p \frac{\partial b_p}{\partial k_m} + h_2 \sum_{p=289}^{338} b_p \frac{\partial b_p}{\partial k_m} + h_3 \sum_{p=339}^{392} b_p \frac{\partial b_p}{\partial k_m} \right.\\
&\left. + h_4 \sum_{p=393}^{450} b_p \frac{\partial b_p}{\partial k_m}\right]\\
&= \sum_{l=1}^{200} \lambda_l s_{lm} + 2[\sum_{j=1}^{125} \left(\sum_{p=201}^{242} s_{pj} s_{pm} + h_1 \sum_{p=243}^{288} s_{pj} s_{pm} + h_2 \sum_{p=289}^{338} s_{pj} s_{pm} + h_3 \sum_{p=339}^{392} s_{pj} s_{pm} \right.\\
&\left. + h_4 \sum_{p=393}^{450} s_{pj} s_{pm} \right) k_j\\
&+ \sum_{j=1}^{81} \left(\sum_{p=201}^{242} c^1_{pj} s_{pm} + h_1 \sum_{p=243}^{288} c^1_{pj} s_{pm} + h_2 \sum_{p=289}^{338} c^1_{pj} s_{pm} + h_3 \sum_{p=339}^{392} c^1_{pj} s_{pm} + h_4 \sum_{p=393}^{450} c^1_{pj} s_{pm} \right) q_{1,j}\\
&+ \sum_{j=1}^{81} \left(\sum_{p=201}^{242} c^2_{pj} s_{pm} + h_1 \sum_{p=243}^{288} c^2_{pj} s_{pm} + h_2 \sum_{p=289}^{338} c^2_{pj} s_{pm} + h_3 \sum_{p=339}^{392} c^2_{pj} s_{pm} \right.\\
&\left. + h_4 \sum_{p=393}^{450} c^2_{pj} s_{pm} \right) q_{2,j}] = 0\,, \qquad m = 1, 2, \ldots, 125\,,
\end{aligned} \tag{B.2}$$

$$\begin{aligned}
\frac{\partial \bar{R}}{\partial q_{1,m}} &= \sum_{l=1}^{200} \lambda_l \frac{\partial b_l}{\partial q_{1,m}} + 2\left[\sum_{p=201}^{242} b_p \frac{\partial b_p}{\partial q_{1,m}} + h_1 \sum_{p=243}^{288} b_p \frac{\partial b_p}{\partial q_{1,m}} + h_2 \sum_{p=289}^{338} b_p \frac{\partial b_p}{\partial q_{1,m}} \right.\\
&\left. + h_3 \sum_{p=339}^{392} b_p \frac{\partial b_p}{\partial q_{1,m}} + h_4 \sum_{p=393}^{450} b_p \frac{\partial b_p}{\partial q_{1,m}}\right]\\
&= \sum_{l=1}^{200} \lambda_l c^1_{lm} + 2[\sum_{j=1}^{125} \left(\sum_{p=201}^{242} s_{pj} c^1_{pm} + h_1 \sum_{p=243}^{288} s_{pj} c^1_{pm} + h_2 \sum_{p=289}^{338} s_{pj} c^1_{pm} \right.\\
&\left. + h_3 \sum_{p=339}^{392} s_{pj} c^1_{pm} + h_4 \sum_{p=393}^{450} s_{pj} c^1_{pm} \right) k_j\\
&+ \sum_{j=1}^{81} \left(\sum_{p=201}^{242} c^1_{pj} c^1_{pm} + h_1 \sum_{p=243}^{288} c^1_{pj} c^1_{pm} + h_2 \sum_{p=289}^{338} c^1_{pj} c^1_{pm} + h_3 \sum_{p=339}^{392} c^1_{pj} c^1_{pm} \right.\\
&\left. + h_4 \sum_{p=393}^{450} c^1_{pj} c^1_{pm} \right) q_{1,j}\\
&+ \sum_{j=1}^{81} \left(\sum_{p=201}^{242} c^2_{pj} c^1_{pm} + h_1 \sum_{p=243}^{288} c^2_{pj} c^1_{pm} + h_2 \sum_{p=289}^{338} c^2_{pj} c^1_{pm} + h_3 \sum_{p=339}^{392} c^2_{pj} c^1_{pm} \right.
\end{aligned}$$

$$+h_4\sum_{p=393}^{450}c_{pj}^2c_{pm}^1\Bigg)q_{2,j}]=0\,, \qquad m=1,2,\ldots,81\,, \tag{B.3}$$

$$\begin{aligned}\frac{\partial\bar{R}}{\partial q_{2,m}}&=\sum_{l=1}^{200}\lambda_l\frac{\partial b_l}{\partial q_{2,m}}+2\Bigg[\sum_{p=201}^{242}b_p\frac{\partial b_p}{\partial q_{2,m}}+h_1\sum_{p=243}^{288}b_p\frac{\partial b_p}{\partial q_{2,m}}+h_2\sum_{p=289}^{338}b_p\frac{\partial b_p}{\partial q_{2,m}}\\&\quad+h_3\sum_{p=339}^{392}b_p\frac{\partial b_p}{\partial q_{2,m}}+h_4\sum_{p=393}^{450}b_p\frac{\partial b_p}{\partial q_{2,m}}\Bigg]\\&=\sum_{l=1}^{200}\lambda_lc_{lm}^2+2[\sum_{j=1}^{125}\Bigg(\sum_{p=201}^{242}s_{pj}c_{pm}^2+h_1\sum_{p=243}^{288}s_{pj}c_{pm}^2+h_2\sum_{p=289}^{338}s_{pj}c_{pm}^2\\&\quad+h_3\sum_{p=339}^{392}s_{pj}c_{pm}^2+h_4\sum_{p=393}^{450}s_{pj}c_{pm}^2\Bigg)k_j\\&\quad+\sum_{j=1}^{81}\Bigg(\sum_{p=201}^{242}c_{pj}^1c_{pm}^2+h_1\sum_{p=243}^{288}c_{pj}^1c_{pm}^2+h_2\sum_{p=289}^{338}c_{pj}^1c_{pm}^2\\&\quad+h_3\sum_{p=339}^{392}c_{pj}^1c_{pm}^2+h_4\sum_{p=393}^{450}c_{pj}^1c_{pm}^2\Bigg)q_{1,j}\\&\quad+\sum_{j=1}^{81}\Bigg(\sum_{p=201}^{242}c_{pj}^2c_{pm}^2+h_1\sum_{p=243}^{288}c_{pj}^2c_{pm}^2+h_2\sum_{p=289}^{338}c_{pj}^2c_{pm}^2\\&\quad+h_3\sum_{p=339}^{392}c_{pj}^2c_{pm}^2+h_4\sum_{p=393}^{450}c_{pj}^2c_{pm}^2\Bigg)q_{2,j}]=0\,,\\&\qquad m=1,2,\ldots,81\,,\end{aligned} \tag{B.4}$$

$$\frac{\partial\bar{R}}{\partial\lambda_m}=b_m=\sum_{j=1}^{125}s_{mj}k_j+\sum_{j=1}^{81}(c_{mj}^1q_{1,j}+c_{mj}^2q_{2,j})=0\,, \qquad m=1,2,\ldots,200\,, \tag{B.5}$$

where Eqs. (B.2)–(B.5) form a system of 487 linear algebraic equations for the determination of the stencil coefficients k_j ($j=1,2,\ldots,125$), $q_{1,j}$ and $q_{2,j}$ ($j=1,2,\ldots,81$) as well as 200 Lagrange multiplier λ_l ($l=1,2,\ldots,200$).

References

[1] S. Vallaghe, T. Papadopoulo, A trilinear immersed finite element method for solving the electroencephalography forward problem, SIAM J. Sci. Comput. 32 (4) (2010) 2379–2394.

[2] R. Crockett, P. Colella, D. Graves, A Cartesian grid embedded boundary method for solving the Poisson and heat equations with discontinuous coefficients in three dimensions, J. Comput. Phys. 230 (7) (2011) 2451–2469.

[3] Q. Zhang, K. Ito, Z. Li, Z. Zhang, Immersed finite elements for optimal control problems of elliptic PDEs with interfaces, J. Comput. Phys. 298 (2015) 305–319.

[4] A. Guittet, M. Lepilliez, S. Tanguy, F. Gibou, Solving elliptic problems with discontinuities on irregular domains - the Voronoi Interface Method, J. Comput. Phys. 298 (2015) 747–765.

[5] P. Huang, H. Wu, Y. Xiao, An unfitted interface penalty finite element method for elliptic interface problems, Comput. Methods Appl. Mech. Engrg. 323 (2017) 439–460.

[6] A. Coco, G. Russo, Second order finite-difference ghost-point multigrid methods for elliptic problems with discontinuous coefficients on an arbitrary interface, J. Comput. Phys. 361 (2018) 299–330.

[7] R. Guo, T. Lin, An immersed finite element method for elliptic interface problems in three dimensions, J. Comput. Phys. 414 (2020) 109478.
[8] K. Li, N.M. Atallah, G.A. Main, G. Scovazzi, The Shifted Interface Method: A flexible approach to embedded interface computations, Internat. J. Numer. Methods Engrg. 121 (3) (2020) 492–518.
[9] C. Gürkan, A. Massing, A stabilized cut discontinuous Galerkin framework for elliptic boundary value and interface problems, Comput. Methods Appl. Mech. Engrg. 348 (2019) 466–499.
[10] Q. Zhang, I. Babuska, A stable generalized finite element method (SGFEM) of degree two for interface problems, Comput. Methods Appl. Mech. Engrg. 363 (2020) 112889.
[11] Y. Xiao, J. Xu, F. Wang, High-order extended finite element methods for solving interface problems, Comput. Methods Appl. Mech. Engrg. 364 (2020) 112964.
[12] A.M. Aragón, B. Liang, H. Ahmadian, S. Soghrati, On the stability and interpolating properties of the Hierarchical Interface-enriched Finite Element Method, Comput. Methods Appl. Mech. Engrg. 362 (2020) 112671.
[13] Y.-C. Yoon, J.-H. Song, Interface Immersed Particle Difference Method for weak discontinuity in elliptic boundary value problems, Comput. Methods Appl. Mech. Engrg. 375 (2021) 113650.
[14] X. Li, X. Zhang, X. Zhou, High order interface-penalty finite element methods for elliptic interface problems with Robin jump conditions, Comput. Methods Appl. Mech. Engrg. 390 (2022) 114505.
[15] Q. Zhang, C. Cui, U. Banerjee, I. Babuska, A condensed generalized finite element method (CGFEM) for interface problems, Comput. Methods Appl. Mech. Engrg. 391 (2022) 114537.
[16] S. Adjerid, I. Babuška, R. Guo, T. Lin, An enriched immersed finite element method for interface problems with nonhomogeneous jump conditions, Comput. Methods Appl. Mech. Engrg. 404 (2023) 115770.
[17] R.J. LeVeque, Z. Li, The immersed interface method for elliptic equations with discontinuous coefficients and singular sources, SIAM J. Numer. Anal. 31 (4) (1994) 1019–1044.
[18] P.A. Berthelsen, A decomposed immersed interface method for variable coefficient elliptic equations with non-smooth and discontinuous solutions, J. Comput. Phys. 197 (1) (2004) 364–386.
[19] S. Yu, G. Wei, Three-dimensional matched interface and boundary (MIB) method for treating geometric singularities, J. Comput. Phys. 227 (1) (2007) 602–632.
[20] A.N. Marques, J.-C. Nave, R.R. Rosales, High order solution of Poisson problems with piecewise constant coefficients and interface jumps, J. Comput. Phys. 335 (2017) 497–515.
[21] F. Tong, W. Wang, X. Feng, J. Zhao, Z. Li, How to obtain an accurate gradient for interface problems? J. Comput. Phys. 405 (2020) 109070.
[22] Y. Ren, S. Zhao, A FFT accelerated fourth order finite difference method for solving three-dimensional elliptic interface problems, J. Comput. Phys. 477 (2023) 111924.
[23] A. Idesman, A new numerical approach to the solution of PDEs with optimal accuracy on irregular domains and cartesian meshes. Part 1: the derivations for the wave, heat and Poisson equations in the 1-D and 2-D cases, Arch. Appl. Mech. 90 (12) (2020) 2621–2648.
[24] A. Idesman, The use of the local truncation error to improve arbitrary-order finite elements for the linear wave and heat equations, Comput. Methods Appl. Mech. Engrg. 334 (2018) 268–312.
[25] A. Idesman, B. Dey, A new 3-D numerical approach to the solution of PDEs with optimal accuracy on irregular domains and Cartesian meshes, Comput. Methods Appl. Mech. Engrg. 354 (2019) 568–592.
[26] A. Idesman, B. Dey, Compact high-order stencils with optimal accuracy for numerical solutions of 2-D time-independent elasticity equations, Comput. Methods Appl. Mech. Engrg. 360 (2020) 1–17.
[27] A. Idesman, B. Dey, Accurate numerical solutions of 2-D elastodynamics problems using compact high-order stencils, Comput. Struct. 229 (2020) 1–18.
[28] A. Idesman, B. Dey, The treatment of the Neumann boundary conditions for a new numerical approach to the solution of PDEs with optimal accuracy on irregular domains and Cartesian meshes, Comput. Methods Appl. Mech. Engrg. 365 (2020) 112985.
[29] A. Idesman, B. Dey, The numerical solution of the 3D Helmholtz equation with optimal accuracy on irregular domains and unfitted Cartesian meshes, Eng. Comput. 38 (2022) 4979–5001.
[30] A. Idesman, B. Dey, New 25-point stencils with optimal accuracy for 2-D heat transfer problems. Comparison with the quadratic isogeometric elements, J. Comput. Phys. 418 (2020) 109640.
[31] A. Idesman, B. Dey, 3-rd and 11-th orders of accuracy of 'linear' and 'quadratic' elements for the Poisson equation with irregular interfaces on unfitted Cartesian meshes, Internat. J. Numer. Methods Heat Fluid Flow 32 (2022) 2719–2749.
[32] A. Idesman, M. Mobin, Optimal local truncation error method for solution of 3-D Poisson equation with irregular interfaces and unfitted Cartesian meshes as well as for post-processing, Adv. Eng. Softw. 167 (2022) 103103.
[33] Wolfram Research, Inc., Mathematica, Version 12.0, URL https://www.wolfram.com/mathematica.
[34] B. Dey, A. Idesman, A new numerical approach to the solution of PDEs with optimal accuracy on irregular domains and cartesian meshes. Part 2: numerical simulation and comparison with FEM, Arch. Appl. Mech. 90 (12) (2020) 2649–2674.
[35] A. Idesman, Optimal local truncation error method for solution of partial differential equations on irregular domains and interfaces using unfitted Cartesian meshes. Review, Arch. Comput. Methods Eng. 30 (2023) 4517–4564.
[36] The MathWorks Inc., MATLAB Version: 9.13.0 (R2022b), The MathWorks Inc., Natick, Massachusetts, United States, 2022, URL https://www.mathworks.com.
[37] O.C. Zienkiewicz, J.Z. Zhu, The superconvergent patch recovery and a posteriori error estimates. Part 1: The recovery technique, Internat. J. Numer. Methods Engrg. 33 (7) (1992) 1331–1364.
[38] O.C. Zienkiewicz, J.Z. Zhu, The superconvergent patch recovery and a posteriori error estimates. Part 2: Error estimates and adaptivity, Internat. J. Numer. Methods Engrg. 33 (7) (1992) 1365–1382.

[39] M. Kumar, T. Kvamsdal, K.A. Johannessen, Superconvergent patch recovery and a posteriori error estimation technique in adaptive isogeometric analysis, Comput. Methods Appl. Mech. Engrg. 316 (2017) 1086–1156, Special Issue on Isogeometric Analysis: Progress and Challenges.
[40] COMSOL Multiphysics V. 6.1, COMSOL AB, Stockholm, Sweden, www.comsol.com.
[41] K.J. Bathe, Finite Element Procedures, Prentice-Hall Inc., Upper Saddle River, New Jersey, 1996.
[42] H.P. Langtangen, S. Linge, Finite Difference Computing with PDEs, Springer, 2017.